UNIVERSITÀ DEGLI STUDI DI PADOVA

Dipartimento di Fisica ed Astronomia "Galileo Galilei"

Corso di Laurea Magistrale in Fisica

Bystander Effects in Photodynamic Therapy of Cancer

Relatore:
Prof. Fabio Mammano

Candidato:
Stefano Ceolin

Correlatore:
Dott. Mario Bortolozzi

Anno Accademico 2013/2014

Contents

Index of Abbreviations

AlPc	Aluminum Phtalocyanine Chloride
L-Arg	L-Arginine
L-Cit	L-Citrulline
Ca^{2+}	Calcium ion
$[Ca^{2+}]_c$	cytosolic free Ca^{2+} concentration
CaB	Calcium Buffer
CaM	Calmodulin
CBX	Carbenoxolone
eNOS	Endothelial NOS
EGTA	Ethylene Glycol-bis(beta-aminoethyl ether)-N,N,N',N'-Tetra-acetic Acid
ER	Endoplasmic Reticulum
FFA	Flufenamic Acid
FMN	Flavin Mononucleotide
FAD	Flavin dinucleotide
fPDT	focal photodynamic therapy
IP_3	Inositol 1,4,5-trisphosphate
iNOS	Inducible NOS
NADPH	Nicotinamide adenine dinucleotide phosphate
NO	Nitric Oxide
NOS	Nitric Oxide Synthase
nNOS	neuronal NOS
NOHA	N^{ω}-hydroxy-L-arginine
PDT	Photodynamic Therapy
PI	Propidium Iodide
PS	Photosensitizer
pSIVA	Polarity Sensitive Indicator of Viability and Apoptosis
ROI	Region Of Interest
ROS	Reactive Oxygen Species
RNS	Reactive Nitrogen Species
H_4B	Tetrahydrobiopterin

Chapter 1

Introduction

Cancer represents the major public health problem for modern society. Despite significant advances in conventional treatment and basic studies providing a better comprehension of cancer biology, only few improvements in therapy efficacy have been reached in the last years. This poor clinical outcome, apart from some notable exceptions, illustrates an unmet clinical need for new therapeutic approaches capable of delivering an effective long-lasting protection against disease recurrence.

1.1 Photodynamic Therapy and Bystander Effects

Photodynamic therapy (PDT) is an approved therapeutic modality, currently used in the treatment of neoplastic and non malignant diseases, which can exert a selective cytotoxic activity toward malignant cells and has the potential to meet many unreached medical needs[3].

The procedure of PDT involves three fundamental components: the photosensitizer (PS), a drug systemically or topically delivered, which remains inactive and produces negligible side effects until photoactivation, the excitation light and molecular oxygen. Together they initiate a photochemical reaction that produces singlet oxygen $^1O_2$, a highly reactive molecule which can cause important and rapid toxicity in target cells leading to apoptosis or necrosis. More specifically, after light absorption, one of the two electrons with opposite spin in the low energy singlet state of the ground state PS is excited into a high-energy orbital. This short-lived species can then decay to the ground state by emitting light or by internal conversion (most PS molecules are fluorescent). Alternatively, the excited singlet state may undergo intersystem crossing to form a relatively long-lived, a few μs, excited triplet-state. The excited triplet state PS can induce chemical changes in a neighbouring molecule via two main pathways, called type-I and type-II photochemical reaction. Firstly, in a type-I reaction, activated triplet state PS can react directly with other adjacent molecules and transfer a proton or an electron to form a radical anion or radical cation, respectively, which may further react with molecular oxygen or nitric oxide (NO) to produce reactive oxygen species (ROS) and reactive nitrogen species (RNS), respectively. Alternatively, in a Type II reaction, the triplet PS can react directly with molecular oxygen(O_2) to form excited

state singlet oxygen[80]. Both Type I and Type II reactions can occur simultaneously, and the ratio between these processes depends on the type of PS used, the concentrations of substrate and O_2[20]. As a result of these photoreactions, cellular organelles and membranes are subjected to photodamage, whose extent and cytotoxicity depends on several independent factors: the type of PS, its extracellular and intracellular localization, the total dose administered, the total light exposure dose and intensity, the oxygenation state of the tissue and the time between the administration of the drug and light exposure.

Photodynamic therapy effects are not restricted to direct cytotoxicity but also involve damage to the tumor vasculature and induction of a robust inflammatory response. Selectivity of this therapeutic approach is derived from the ability of the PS drug to accumulate in tumor environment and light delivery to the tumor locus. The treatment does not produce changes in tissue temperature leading to minimal fibrosis and preserving mechanical integrity of hollow organs undergoing PDT. Minimal side effects on normal tissue and lack of resistance mechanism make this approach a valuable therapetic option[3].

Cell death and the bystander effect are crucial for both the efficacy of cancer therapy and the modulation of anti-tumor immune response. The effect refers to a process whereby untreated cells exhibit either the deleterious or beneficial indirect effects as a result of signals received from nearby targeted cells[9].Various molecular players and pathways have been suggested to mediate the bystander effects, nevertheless to date it is not known which are the key molecules and cellular mechanisms underpinning cell death signal propagation. Several reports suggest the involvement of both NO and RNS in mediating the bystander effect. Nevertheless their role in the process has not been totally defined since these molecules can either inhibit or sustain tumor progression. From a molecular point of view, radiation-induced bystander response is based on two main mechanisms of action, which involve both directly contacting cells via gap junctions and not physically connected cells through the release of soluble factors. These factors, preferentially transferred through extracellular medium from irradiated to non irradiated cells, include lipid peroxide products, inosine nucleotides and cytokines such as tumor necrosis factor-α (TNFα). Reactive oxygen species (ROS), such as superoxide radicals, are also involved in bystander cell signals[82]. Furthermore, a growing number of findings support the importance of NO in intercellular signal transduction pathways initiated by ionizing radiation.

1.2 Nitric Oxide as a signalling molecule

NO is a short lived, ubiquitous free radical gas with a key role in many physiological and pathological processes. Its role as a signalling molecule was first determined as the endothelium derived relaxing factor in 1987[41].

NO is synthesized by Nitrix Oxide Synthase enzymes (NOS) from arginine and O_2 in both Ca^{2+}-dependent or independent ways, depending on wich enzyme is involved. Three different NOS enzyme are present in mammals: nNOS (also known as Type I, NOS-I and NOS-1 being the first isoform found) predominating in neuronal tissue; iNOS (also known as Type II, NOS-II and NOS-2), which is inducible in a wide range

of cells and tissues, primarily in macrophages; and eNOS (also known as Type III, NOS-III and NOS-3) predominantly found in endothelial cells[50]. These different enzymes are products of different genes, with different localization, regulation, catalytic properties and inhibitor sensitivity, and with 51-57% homology between the human isoforms, suggesting the existence of a common ancestral NOS gene.

The importance of NO as signalling molecule and its biological effects have now been characterized in a number of tissues. Smooth muscle relaxation is an important function for NO, playing a key role in blood vessels vasodilation. NO synthesis from nNOS and its importance in neurotransmission is also well established both peripherally[104] and centrally in the process of long term potentiation or depression[93]. In particular, NO produced by eNOS and nNOS is released for short periods of time and acts as a transduction mechanism whereas NO released from iNOS after activation of macrophages by cytokines is synthesized for long periods and acts as a cytotoxic molecule for invading microorganisms and tumor cells[87]. NO plays also a role in cellular respiration regulation, as nanomolar concentrations of NO reversibly inhibit cytochrome oxidation and mitochondrial respiration. Higher concentrations of NO can irreversibly inhibit the respiratory chain leading to PTP opening and cell death[17].

Before the discovery of NO physiological production by NOS, NO was considered a pollutant. It's now clear that the physical properties of NO make it particularly well suited to its role as a signalling agent, diffusion coefficient for NO in aqueous solution is reported to be 3300 $\mu m^2/s$ [65]. The relatively long lifetime of NO, despite its radicalic nature, allows it to reach neighbouring target cells. NO is then oxidized to NO_3 and NO_2 under physiological conditions, thus no separate mechanism for its destruction is required.

The main receptor for NO in target cells is the soluble isoform of guanylate cyclase (sGC), one of the two enzymes that produce cGMP and the only definitive receptor for NO. For this reasons, sGC is intimately involved in many signal transduction pathways in the cardiovascular and nervous system[43]. sGC is a heterodimeric protein composed of α and β subunits. The β-subunits contains a ferrous heme group that is a highly selective receptor for NO. Activation of the sGC by NO induces a 300-fold increase in its activity[67] producing a burst of cGMP. The rise in cGMP concentration allow sGC to transmit a NO signal to cGMP dependent protein kinase, cGMP-dependent cation channels and cGMP-dependent phosphodiesterase. cGMP-dependent kinases in turn produce a lowering of intracellular Ca^{2+}, leading to effects such as smooth muscle relaxation.

1.3 Nitric Oxide Synthases: structure and function

NOS activation is strictly dependent on enzyme structure and shows remarkable differences between different isoforms. Importantly, the activities of all isoforms depend on their binding to calmodulin(CaM).

To become active each NOS enzyme must assemble in a dymeric structure of two subunits[27]. Each subunit in a NOS dymer exhibit an N-terminal oxygenase domain that binds a heme group, a tetrahidrobiopterin cofactor and the substrate arginine. Additionally, the C-terminal reductase domain binds flavin mononucleotide (FMN),

flavin adenine dinucleotide (FAD), and nicotinamide adenine dinucleotide phosphate (NADPH). Between these domains a CaM binding site of 20-25 amminoacids is found. CaM bound to NOS plays a key role in NO synthesis by allowing electron transfer to the heme group. When the CaM-NOS dymer is assembled, electron transfer starts from NADPH, proceeds through FAD and FMN in one dymer. Electrons are then transfered to the heme group on the second subunit, as shown in figure 1.1. CaM intervene in the process facilitating both intra-domain and inter-domain electron transfer[67].

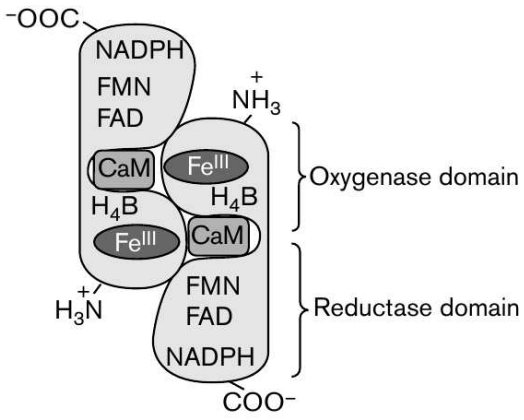

Figure 1.1: NOS dymeric structure scheme[45]

CaM is a small Ca^{2+} binding protein formed by two lobes that contains two E-F hands each one[52] capable of bind two Ca^{2+} in a cooperative way, providing on the whole four Ca^{2+} binding sites. After Ca^{2+} binding, CaM can activate more than 30 different enzyme. Fully activation of target proteins by CaM typically requires occupancy of all four Ca^{2+}-binding sites. CaM binds to each NOS subunit in a 1:1 stoichiometry but with different affinities depending on NOS type. iNOS display a considerable higher affinity for CaM then eNOS and nNOS. Moreover iNOS binds CaM even in absence of Ca^{2+}, whereas eNOS and nNOS bind CaM only in presence of Ca^{2+}. Dissociation of Ca^{2+} from bound CaM takes place in two steps. First, rapid Ca^{2+} dissociation from CaM N-terminal lobe leads to NO synthesis blockage. Then a slower Ca^{2+} dissociation from the C-terminus occurs and CaM dissociates from NOS[79][18].

As mentioned above CaM regulates NOS activity by controlling electron transfer to the heme group. This effect is due to a conformational rearrangement that sets the FMN subdomain in closer proximity to the oxygenase heme domain and involve two regulatory elements of the enzyme[103].

Autoinhibitory loop is a regulatory element unique of eNOS and iNOS. It consists of a 40-50 amino acid insert in the FMN binding module that is not present in iNOS. Similar structures have been reported also in a number of CaM activated enzymes. Deletion of this insert in eNOS and iNOS reduces EC_{50} for Ca^{2+}-saturated CaM and also enables some residual NO synthesis in the absence of CaM, confirming the function of this structure and its contribution to Ca^{2+} dependence of eNOS and nNOS. How this

inhibitory element inhibits enzyme activity is not completely clear, however enzyme activation is fully dependent on a movement of the autoinhibitory insert, which could be affected by the Ca^{2+}-saturated CaM.

Another unique regulatory element of eNOS and nNOS is the C-terminal extension, formed by a tale of 20-40 amino acids. Deletion of different residues from eNOS and iNOS extension accelerates electron transfer into flavins domain and also leads a lower Ca^{2+} dependence and an increase in catalytic activities. Importantly, a phosphorylation site in the C-terminal extension can modulate Ca^{2+} dependence of the enzyme. In the absence of CaM, the C-terminal extension covers the NADPH, FMN and FAD subdomain of the enzyme preventing electron transfer to the redox partners[7].

Thus, the autoinhibitory loop and the C-terminal tail inhibit the activity of eNOS and iNOS in the absence of Ca^{2+}-saturated CaM. Other structural elements along with protein phosphorylation also regulate Ca^{2+}/CaM binding and tune enzyme activity[4].

When CaM is bound, NOS catalyze the redox convertion of L-arginine (L-Arg) in L-citrulline (L-Cit) and NO through a complex reaction pathway that can be divided in two major steps with N^{ω}-hydroxy-L-arginine (NOHA) as intermediate product[94]:

$$\text{L-Arg} + O_2 + \text{NADPH} \longrightarrow \text{NOHA} + \text{NADP}^+ \tag{1.1}$$

$$2\,\text{NOHA} + O_2 + 2\,\text{NADPH} \longrightarrow 2\,\text{L-Cit} + \text{NADP}^+ + \text{NO} \tag{1.2}$$

The essential role of FAD and FMN cofactors in the reductase domain is to accept two electrons from NADPH and pass them on to a one-electron acceptor heme domain by forming stable semiquinone radical intermediates. The monooxygenase II step involves the reduction of heme ferric to ferrous ion and O_2 binding. This form of the enzyme then reacts with N^{ω}-hydroxy-L-arginine to form its radical and a heme-peroxy complex. The N^{ω}-hydroxy-L-arginine radical and the peroxy complex then react with each other in a 'radical rebound' mechanism to generate citrulline and NO, and to regenerate the ferric haem iron.

1.4 Non-enzymatic Nitric Oxide production

In addition to the well known generation from NOS, new studies over the last years have demonstrated additional mechanisms for NO production in biological tissues. The first evidence of NOS/L-Arg independent NO synthesis was reported in ischaemic heart by direct reduction or disproportionation of nitrite (NO_2^-) to NO under acidotic and highly reduced conditions[55].

Further studies have confirmed the role of nitrite as an important storage form of NO that can be released in a complete enzyme-independent pathway; moreover correlative EPR measurements of NO and P-NMR measurements of intracellular pH demonstrated that the magnitude of NO generation from nitrite increases as the pH of the tissue decreases[55]. The magnitude of nitrite disproportionation process was also quantitatively characterized by means of EPR and chemiluminescence studies and the corresponding rate law of NO formation was obtained. The reaction scheme proposed for this process by Zweier et al.[54] involves the equilibrium that takes place between NO_2^- and nitrous acid (HNO_2) under acidic conditions. Nitrous acid in turn exists in

equilibrium with nitrosonium acid(NOOH) which can react with NO_2^- to give N_2O_3 an subsequently NO. The rate of NO production by this process was estimated to be:

$$\frac{d[\mathrm{NO}]}{dt} = \frac{k_1[\mathrm{NO_2^-}][\mathrm{HNO_2}]}{[\mathrm{NO_2^-}] + k_\beta} \tag{1.3}$$

where $[HNO_2]$ can be related to initial nitrite concentration and $[H^+]$. Under physiological pH and nitrite concentration a small rate of NO production of 0.5pM/s is predicted whereas when pH falls down at values as low as 5.5, NO production can reach a rate of tens of nM/s[54].

Several other reactions have been shown to lead to NOS-independent NO production that include the reduction of nitrite to NO catalyzed by microbial nitrite reductase and xanthine oxidoreductase under hypoxic conditions. Moreover the mitochondrial respiratory chain and also other heme containing enzymes can take part in nitrite reduction[97]. Finally, hydrogen peroxyde reacting with L-Arg or similar compound was reported to be involved in NO production[74].

Of particular relevance for PDT, it was recently reported that aluminum phthalocyanine (AlPc), a common PS used also in our experiments, can buffer NO and can be used as a NO carrier in biological system. As shown by Silva et al.[91] NO complexation to AlPc depends on the oxidation state of the latter. Particularly, NO binds more strongly to AlPc in the reduced state than in the oxidized state. These studies suggest that AlPc can act as a store for NO that can be released during the PS oxidation that takes place following photoactivation.

1.5 The dual role of nitric oxide in cancer biology

At physiological concentration NO acts as a signal molecule in many processes, such as blood flow regulation, smooth muscle relaxation, iron homeostasis, platelet reactivity and neurotransmission[56]. At higher concentrations, NO provides cytotoxic defensive mechanisms against pathogens and tumors[72]. In general, high NO/RNS are thought to exert a pro-apototic action[106]. Both NO and RNS induce post translational modification in target proteins, block cellular respiration interfering with the electron transport chain in the mitochondria resulting in cytochrome C release and apoptosis initiation[57]. High NO concentration can also cause DNA damage that can both start oncogenesis or induce apoptosis in cancer cells. Despite these effects NO role in cancer teraphy is strongly debated as, some cases, NO can promote tumor growth and resistance. An example of this dual role is inhibition of cell death by S-nitrosation of the active site cysteine residue in caspases[28]. Moreover, it has been reported that tumors producing high level of NO or incubated with NO donors show a decrease in cell death after photosensitization[35].

1.6 Calcium signalling in cancer

Ca^{2+} ion is a ubiquitous intracellular signalling molecule that is required to regulate a large variety of cell processes like fertilization, cell proliferation and differentiation,

transcription factor activation and apoptosis modulation[13]. Due to its ubiquity and versatility, Ca^{2+} probably plays an important role as a signalling agent also in cancer cells, where Ca^{2+} signalling networks could be remodelled because of altered expression of key elements of the so-called Ca^{2+} signalling toolkit[77].

The latter comprises channels, pumps and receptors that together modulate Ca^{2+} dynamics generating complex spatio temporal organized signalling patterns. At rest, the cytosolic free Ca^{2+} concentration ($[Ca^{2+}]_c$) is about 100 nM. This low basal level can be rapidly increased by Ca^{2+} influx from the extracellular medium, where Ca^{2+} concentration typically about 1 mM. A rapid rise of $[Ca^{2+}]_c$ can be also triggered by release of Ca^{2+} from internal stores, like endoplasmic reticulum (ER), mitochondria, Golgi apparatus and lysosomes and also from Ca^{2+} buffer proteins. Influx of Ca^{2+} from the extracellular mileau is mediated by different channels that can be divided into three main family: the voltage operated channels (VOCs) which open in response to membrane depolarization, the receptor operated channels(ROCs) which open in response to the extracellular binding of a ligand and the store operated channels (SOCs) that is activated by depletion of intracellular stores. Ca^{2+} release from the ER is mediated by receptor operated channels, particularly ryanodyne and inositol 1,4,5-trisphosphate (IP_3) receptors on the endoplasmic reticulum[85].

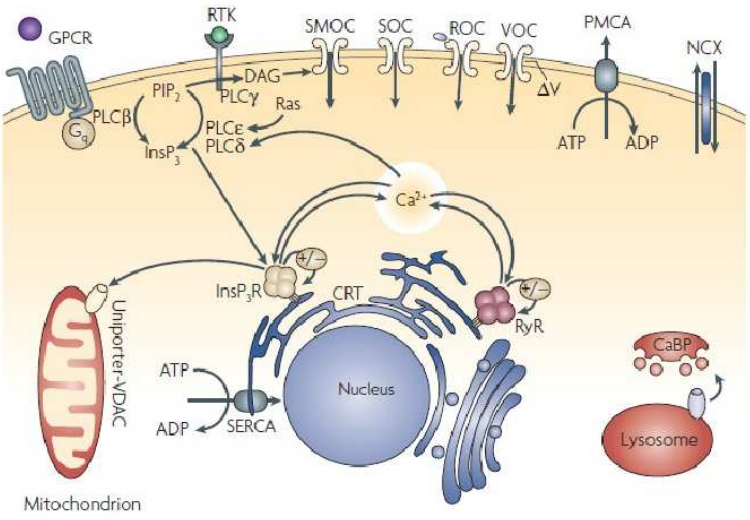

Figure 1.2: Ca^{2+} dynamics pathways

After surging in response to a stimulus, $[Ca^{2+}]_c$ is rapidly reduced to the resting level by exchangers, like the Na-Ca exchangers, and pumps, like Ca^{2+}-ATPases (PMCA) in the plasma membrane and sarco-endoplasmic reticulum ATPases(SERCA) in the ER. Also mitochondria, through the mitocondrial calcium uiporter (MCU), and the Golgi apparatus and lysosomes through secretory pathway Ca^{2+}ATPases, can contribute to reduce $[Ca^{2+}]_c$ after a stimulus[48].

Peculiarities of Ca^{2+} dynamics in cancer cells emerge from deregulation of one or more of these toolkit components. The most dysregulated channels identified in hu-

man tumors are TRPM8, ORAI1 and TRPV6 which are upregulated in prostate, breast and colon cancers; SERCA2 is downregulated in lung, colon and thyroid tumors and PMCA, whose isoforms are deregulated in breast, lung colon and oral neoplasia[42]. Moreover, ORAI1 and TRPM7 are reported to be overexpressed in human breast cancer where they promote tumor cell migration, invasion and metastasis[24] and ATP2C1 and ATP2C2 are upregulated in breast cancer. This alterations could affect Ca^{2+} signalling in cancer cells modulating the resting Ca^{2+} concentration in the cytoplasm, ER and other stores. Either the overexpression of protein like IP_3R channels that cause Ca^{2+} leakage from ER, or the lower expression of SERCA, reducing Ca^{2+} sequestration can cause a lower level of endoplasmic reticulum Ca^{2+} content. This fact could lead to a decrease in apoptotic cell death of cancer cells because Ca^{2+} release from ER and subsequent uptake from mitochondria play a key role in trigger apoptosis.

Summary

The aim of this study is to cast new light on the role of NO and Ca^{2+} in bystander effect propagation during PDT. Prior works suggests the involvement of NO and RNS in bystander effect but only indirect evidences of their role were reported. The first goal of our work was to verify the onset of NO signals in PDT, dynamically monitoring its concentration in real-time with the novel NO probe CuFl. Simultaneously Ca^{2+} imaging, achieved with the widely used Ca^{2+} probe Fura-2, was also used to investigate the association between Ca^{2+} and NO signals.

Experimental methods and materials used in imaging experiments are described in chapter 2, where a new method to accurately analyze CuFl fluorescence is introduced, allowing the observation of real-time NO dynamics.

Our data, presented in the first section of chapter 3, provides the first direct evidence of NO involvement in PDT. Moreover, simultaneous imaging shows the NO signals in bystander cells spatially and temporally associated to an intercellular Ca^{2+} wave. The shape of NO signals suggests a dual mechanism that involves direct release from the target cell as well as enzymatic production.

In the second section of chapter 3 we develop a mathematical model of NO diffusion from target to bystander cells, in order to estimate the contribution of the diffusive component relative to the enzymatic production. Afterwards, we introduce a comprehensive description of NO production from NOS caused by Ca^{2+} transients, that could be divided in two major steps: the activation of the enzyme and the NO synthesis process. For the latter we refer to previously reported models whereas for Ca^{s+} mediated activation of the enzyme we present a new mathematical description based on experimental data reported in literature. The reliability of the overall model was tested by comparing significant parameters predicted by simulations with corresponding values found in literature.

The final goal of this study was to use our model of eNOS activation to predict NO production rate in response to Ca^{2+} signals recorded in PDT experiments. Results are shown at the end of chapter 3 and suggest that this model of eNOS activation and NO production accounts for the rapid NO production caused by PDT, but fails to predict subsequent enzyme inactivation. These results also suggest that local Ca^{2+} dynamic is crucial to modulate NO production.

Chapter 2

Experimental Methods and Materials

2.1 Cell culture

C26GM mouse colon carcinoma cells line, previously described by Bronte et al.[16], were grown in DMEM (Invitrogen), supplemented with 2mM L-glutamine, 10mM HEPES, 50 μM 2-Mercaptoethanol, 150 U/mL streptomycin, 200 U/mL penicillin, and 10% heat-inactivated FBS (Gibco). For in vitro studies, 1.5-2.0 x 10^5 C26GM were plated on 12mm round glass coverslips into 24-well culture plates.

2.2 In vitro PDT, ratiometric calcium imaging and NO imaging

Aluminum phthalocyanine chloride (AlPC) (Sigma) was dissolved in dimethyl sulfoxide (Sigma) at (10 mM) and kept in the dark. C26GM cell cultures were incubated with AlPC (10 μM) and co-loaded with Fura-2 AM (15 μM) (Molecular Probes) for 60 min at 37° in DMEM containing pluronic F-127 (0.01%, w/v), and sulphinpyrazone (250 μM). For NO detection, after one hour of AlPC and Fura-2 incubation, cells were loaded with CuFl (20 μM) for 20 min at room temperature. C26GM cells were then transferred to the stage of an upright spinning-disk confocal fluorescence microscope and continually superfused with an extracellular medium containing NaCl (150mM), KCl (5mM), $MgCl_2$ (1mM), Sodium Pyruvate (2mM), Hepes-NaOH (10mM), D-glucose (5mM) (pH 7.2, 310 mOsm). When present, $CaCl_2$ was added at the final concentration of (1mM).

For focal photosensitization, the output of a 671nm solid state laser was injected into a permissive fibre optic cable (62.5 μm core, Thorlabs), whose output was projected onto the specimen plane by an aspheric condenser lens (20 mm effective focal length, Thorlabs) and the recollimated beam was directed onto a dichromatic mirror (650 shortpass, Edmund Optics) placed at 45° just above the objective lens of the microscope. By carefully adjusting the position of the fiber in front of the aspheric lens we projected a sharp image of the illuminated fiber core (spot) onto the specimen focal plane selected by the objective. For focal PDT treatment, an irradiation time of 60 sec

was used to deliver 0.06 mW/μm^2 of light (Power = 5 mW centered on a circular area of 80 μm^2) from the 671 nm solid state laser, using a 40X water immersion objective (N.A.= 1.15, UApoN340, Olympus).

Fura-2 fluorescence was alternatively excited at 365 nm and 385 nm by light from collimated high power LEDs(M365L and M385L, respectively; Thorlabs) filtered though 15 nm interference band-pass filters and directed onto the sample through a DM480HQ dichromatic mirror (Olympus). Fluorescence emission was selected using an interference filter (BA495-540HQ, Olympus) to form fluorescence images on a sCMOS camera (PCO.Edge). Images were recorded on at a rate of 1 frame pair per second. Signals were measured as dye emission ratio changes, $\triangle R = R(t) - R(0)$, where t is time and $R(t)$ is emission intensity excited at 365 nm divided by the intensity excited at 385 nm, and $R(0)$ indicates pre-stimulus ratio. Estimates of $[Ca^{2+}]_c$ were made from ratio values by application of the Grynkiewicz equation[37]

$$[Ca^{2+}]_c = \frac{k_d(R - R_{min})}{R_{max} - R}\left(\frac{F_f}{F_b}\right) \tag{2.1}$$

Symbol definition and details on fluorescence Ca^{2+} imaging based on dual wavelength indicators are provided in appendix B on page 61. Calibration procedure and details are described in the next section.

For NO detection, after one hour AlPC incubation, cells were loaded with the novel selective fluorescent probe, 2-4,5-Bis[(6-(2-ethoxy-2-oxoethoxy) -2-methylquinolin-8-ylamino)methyl] -6-hydoxy-3-oxo-3H-xanthen-9-yl benzoic acid Fl_5 (CuFl)[58] at the final concentration of (20 μM) (Strem Chemicals). Cells co-loaded with AlPC, CuFl (and eventually also Fura-2 for combined imaging experiments) were excited using a collimated 470 nm LED (M470L2–C1, Thorlabs). Signals were measured as relative changes of fluorescence emission intensity ($\triangle F/F_0$), where F_0 is prestimulus fluorescence, F is fluorescence at post–stimulus time t and $\triangle F = F–F_0$. Since CuFl is an irreversible fluorescent indicator an estimate of NO concentration can be be derived from the temporal derivative of relative changes in fluorescence emission:

$$[NO](t) \simeq \frac{\dfrac{d}{dt}\left(\dfrac{F(t)}{F_0}\right)}{k_{fluo}\left(13.14 - \dfrac{F(t)}{F_0}\right)} \tag{2.2}$$

as described in section 2.4 on the facing page.

Images were recorded at a rate of 1 couple of frame/second for Fura-2 and 1 frame/second for CuFl, (camera exposure time 50ms/frame). Pharmacological interference experiments with EGTA (100μM) (adjusted to pH 7.3 with NaOH), U73122 (2.5μM) and Flufenamic Acid(FFA) (100μM), Probenecid(200μM), 2-APB(100μM), Suramine (200μM) and CBX(100μM) were performed by adding the reagents in extracellular medium bath at room temperature.

In order to assess possible direct effects of AlPc or its photo-activation by-products on Fura-2 or CuFl fluorescence emission, experimental tests were carried on in small

aqueous vesicles dipersed in Sylgard[19]. In these conditions, AlPc photo-activation did not induce changes in CuFl fluorescence emission and caused a negligible increase in Fura-2 emission both at 360nm and 380nm excitation wavelengths. Details are shown in section C.2 on page 64.

2.3 Time-lapse microscopy of apoptosis triggered by focal PDT with AlPC

C26GM cell were co-loaded with AlPC and fura-2 as described above. After focal (single cell) photosensitization, pSIVA-IANBD and Propidium Iodide (Imgenex) were added directly to the extracellular medium enriched with $CaCl_2$ to the final concentration of (2.5 mM) and cells were imaged by time-lapse microscopy for up to 4 hours. pSIVA-IANBD fluorescence was excited at 470 nm and fluorescence emission was selected using an interference filter. Propidium Iodide was illuminated by a 535 nm LED, through a DM560 dichromatic mirror (Olympus), and fluorescence emission was collected through a long-pass emission filter (590LPV2, Olympus).

2.4 CuFl fluorescence emission

CuFl is a novel turn-on fluorescent cell-permeable probe designed to visualize NO in living cells. Unlike previously reported NO fluorescent sensors, CuFl directly and immediately images NO rather than its derivative species and it can spatially distinguish which cells are producing NO. This highly sensitive proble can yield a fluorescence increase up to 16-fold in the presence of excess NO[59]. The fluorescence response of CuFl to other reactive species is negligible, with the relevant exceptions of $ONOO^-$ and O_2^- which cause a fluorescence increase of 2.6-fold and 2-fold respectively (figure 2.1 (b)).

The mechanism responsible for NO sensing by CuFl is based on the coordination of a fluorophore ligand to a metal ion to quench the fluorescence, which is restored by NO reduction of the metal center with release of the nitrosated ligand. This process occurs irreversibly[58][69] and is described by the following reaction scheme[59]:

$$\mathrm{Fl} + \mathrm{Cu^{II}} \longleftrightarrow \mathrm{Cu^{II}(Fl)} \tag{2.3}$$

$$\mathrm{Cu^{II}(Fl)} + \mathrm{NO} \longrightarrow \mathrm{Cu^{I}} + \mathrm{FlNO} \tag{2.4}$$

With reference to our experimental setup configuration, CuFl fluorescence emission was collected in the range from 500 nm to 540nm, resulting in an effective 14.14 fold emission increase. Fluorescence emission of CuFl can be related to the fluorophore concentration by means of the proportionality constant S. Therefore the total emission recorded at every instant is:

$$F(t) = S[\mathrm{CuFl}](t) + 14.14S[\mathrm{FlNO}](t) \tag{2.5}$$

Let us define F_0 as fluorescence emission at time t_0, the time in which the experiment data recording starts. At such time a small fraction of loaded CuFl already reacted

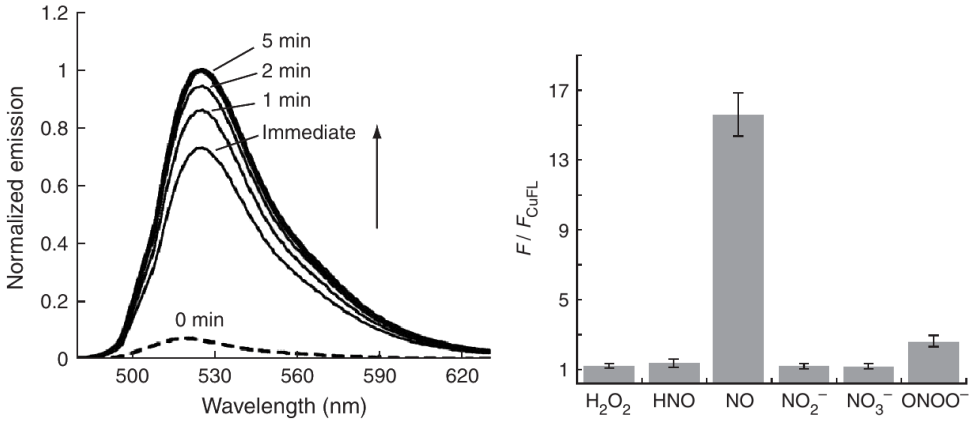

Figure 2.1: (a) Fluorescence emission spectra of a solution of CuFl upon addition of NO (1.3 mM) (b)Specificity of CuFl for NO over other species. All data are normalized with respect to the emission of CuFl (Reproduced from Ref.[59]).

with NO giving rise to FlNO, therefore the fluorescence emission is due to both species but the latter results negligible:

$$F_0 = S[\text{CuFl}](t_0) + 14.14S[\text{FlNO}](t_0) \simeq S[\text{CuFl}](t_0) \tag{2.6}$$

and the normalized fluorescence emission results

$$\frac{F(t)}{F_0} = 1 + 13.14\frac{[\text{FlNO}](t)}{[\text{CuFl}](t_0)} \tag{2.7}$$

Given that the reaction between NO and CuFl occurs irreversibly, fluorescence emission at a particular instant does not directly represent NO concentration. However it is possible to relate such concentration to the rate of increase of fluorescence signal. Indeed, consistently with reaction 2.4, the rate of $Fl_5{-}NO$ formation is:

$$\frac{d[\text{FlNO}](t)}{dt} = k_{fluo}[\text{NO}](t)[\text{CuFl}](t) = k_{fluo}[\text{NO}]\left([\text{CuFl}](t_0) - [\text{FlNO}]\right) \tag{2.8}$$

where the rate constant k_{fluo} of the reaction has been introduced. Similarly we could calculate the derivative of the normalized fluorescence emission:

$$\frac{d}{dt}\left(\frac{F(t)}{F_0}\right) = 13.14\frac{k_{fluo}[\text{NO}](t)[\text{CuFl}](t)}{[\text{CuFl}](t_0)} \tag{2.9}$$

and obtain an estimate of NO concentration through the last relation:

$$[\text{NO}](t) = \frac{\dfrac{d}{dt}\left(\dfrac{F(t)}{F_0}\right)}{k_{fluo}\left(13.14 - \dfrac{F(t)}{F_0}\right)} \tag{2.10}$$

In order to estimate NO concentration the value of the rate constant k_{fluor} should be known. Unfortunately such value has not been reported in literature yet, therefore NO concentration presented in this work will be expressed as $[\text{NO}]k_{fluor}$.

2.4.1 Numerical analysis of CuFl data

In order to estimate NO concentration from raw fluorescence data, equation 2.10 must be evaluated, particularly numerical differentiation of fluorescence data series is the critical computation step.

Assuming that we can model recorded data F as the superposition of real fluorescence values $\tilde{F}$ with a white noise term gives:

$$\frac{F(t_i)}{F(t_0)} = \frac{\tilde{F}(t_i)}{\tilde{F}(t_0)} + N(0, \sigma) \tag{2.11}$$

where we have normalized our data to fluorescence emission at t_0, estimated as the mean fluorescence emission during the first ten seconds of recording.

Facing the task of numerical differentiate a data series, one could be tempted to use a local method like simple finite difference:

$$\frac{dF}{dt} \simeq \frac{F(t_{i+1}) - F(t_{i-1})}{2\delta t}$$

but such procedure greatly amplify noise on derivative estimates that results $\frac{\sigma}{\sqrt{2}\delta t}$. Widely used procedures to avoid noise amplification are the so called global methods[47]. Such methods yield an estimation $f(t)$ of the data on the whole time interval by means of least square minimization and then analytically differentiate it.

In practice recorded data was divided in two dataset, the first one consist of signal baseline until photoactivation that take place at 30s, the second from photoactivation to the end of recording. Both samples were interpolated with a least square polynomial of order N_1 and N_2, setted to $N_1 = 2$ for the first dataset and $N_2 = 10$ for the second one in order to reduce noise without originate artefacts. The interpolating polynomial in the second data set was also constrained to be continuous with the first one.

2.5 Data analysis and statistics

Images, acquired using software developed by Prof. Mammano's group, were analyzed based on Matlab platform (Release 14, MathWorks, Inc., Natick, MA, USA). Specific regions of interest (ROIs), corresponding to different cells located at different distance from the PDT-targeted cell, were drawn in order to measure the mean fluorescence traces of Fura-2 and CuFl signals per single cell obtained as the mean fluorescence value on every ROIs area at every instant. Specifically, for statistical analysis of the bystander effect, we have selected an annulus, centred on the target cell, with an inner radius of 75 μm and an outer radius of 120 μm. In such region 36 randomly selected cells were considered.

In order to compare different experiments and drugs effects the amplitude of Ca^{2+} and NO signals in the annular region and the Ca^{2+} wave speed were chosen as the most significant parameters. Amplitude was measured as maximal Ca^{2+} or NO concentration variation in response to a specific stimulus. Unless otherwise stated, statistical comparisons of means for paired samples were made by one-way heteroscedastic

Student t-test. p-values are indicated by letter p and $p < 0.05$ was selected as the criterion for statistical significance. In figures, asterisks were used as follows: * $p \leq 0.05$; ** $p \leq 0.01$; *** $p \leq 0.001$.

Pseudocolor images were generated using the hue-saturation-value (HSV) visualization algorithm: hue was used to represent fluorescence changes; value (brightness) carried pixel intensity from a reference image that was either updated on a frame-by-frame basis or obtained as an average over a specified number of frames; saturation was set to 1.0. Frames so constructed were converted to ordinary RGB images by a single call to the Matlab library function hsv2rgb, and displayed.

Chapter 3

Results

3.1 Experimental Results

3.1.1 Calcium and Nitric Oxide: bystander signals in PDT

Radiation induced bystander effects have become established in the radio-biology vocabulary but key messengers and signalling pathways are only partially characterized. Several reports suggest the involvement of NO and RNS in bystander effects, even if no direct evidence of NO release after PDT has been published. Chemiluminescence and spectroscopy have been used for NO tracking, however these methods suffer from low spatial and temporal resolution and, in some cases, require complicated instrumentation.

Small molecule–based fluorescent probes for NO, including o-diaminonaphthalene (DAN), o-diaminofluoresceins (DAFs) and o-diaminocyanines (DACs), are now commercially available, but their changes in fluorescence require reactions with oxidized NO products rather than NO itself, thus, their fluorescence-response does not necessarily reflect real-time NO production. For these reasons, we based our studies on CuFl that is substantially more selective for NO compared to other potentially interfering molecules and can be utilized to visualize NO production in living cells with a high spatial and temporal resolution[58].

To single out the key mediators of bystander effects and to define the role of NO, imaging experiments were performed on C26GM colon cancer cell monolayers grown on glass coverslips and co-loaded with the PS AlPC. Drug photoactivation was restricted to a single cell of the culture by focusing 670nm laser light into an 80 μm^2 circular area. We refer to this type of stimulation as *focal PDT* (fPDT).

Since NOS activation may depend on intracellular Ca^{2+} concentration, which is known to modulate a plethora of cellular processes and is also involved in cell death, we took advantage of the ratiometric Ca^{2+} indicator Fura-2 to monitor intracellular Ca^{2+} level variations.

As shown in figures 3.1 and 3.2, fPDT evoked a rapid increase in intracellular Ca^{2+} concentration and induce a Ca^{2+} wave that propagates from target cell invading the whole field of view (corresponding to an area of $6 \cdot 10^4 \mu m^2$). Simultaneously, an extremely fast NO release from target and bystander cells is observed. These

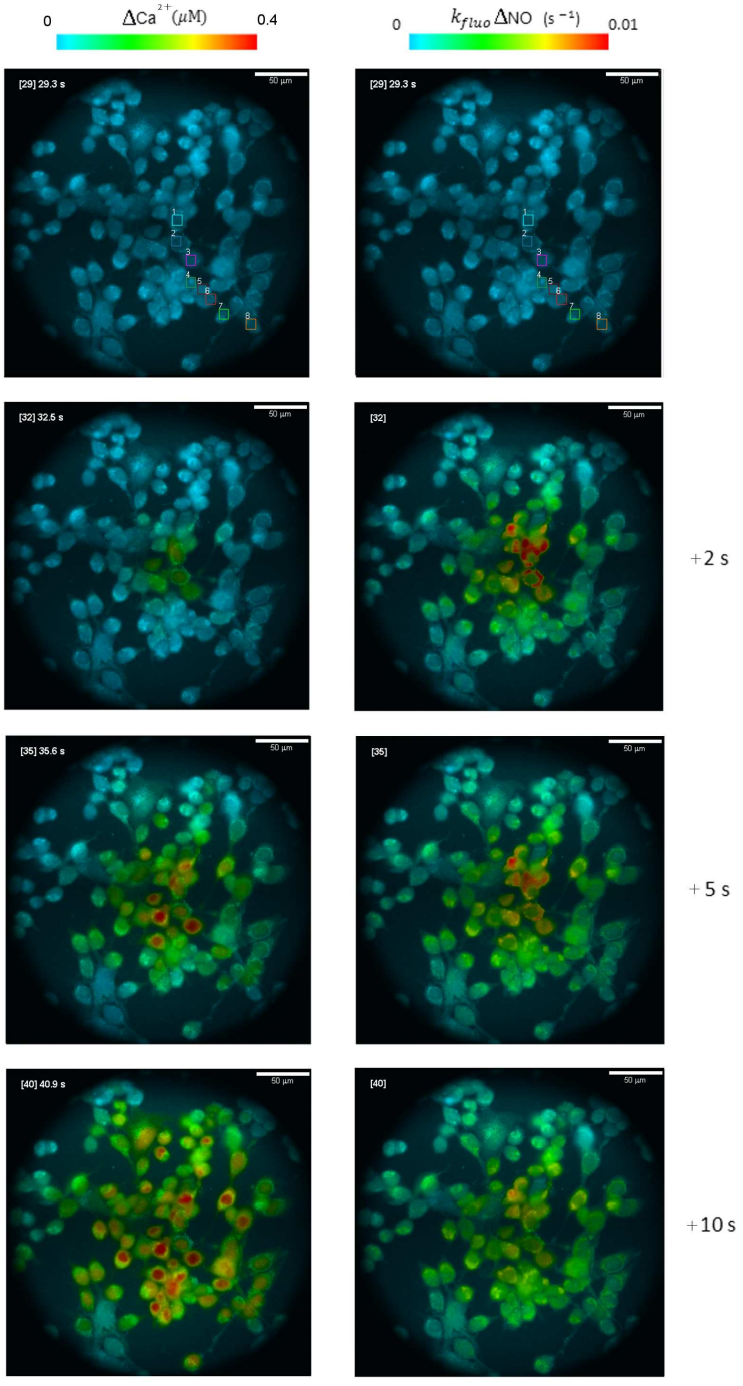

Figure 3.1: Representative false-color images of Ca^{2+} and NO concentration during PDT in control C26GM cells, encoded as shown in the color scale bar. NO signals were expressed as a function of k_{fluo}(see methods). Images illustrate the sample before 1-min AlPc photoactivation and after +2, +5 and +10 s from laser turn on.

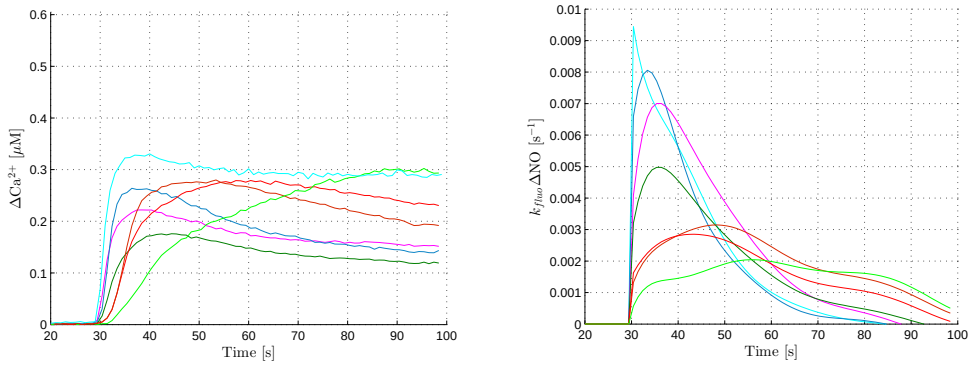

Figure 3.2: NO and Ca^{2+} traces obtained within 7 regions of interest (ROIs) corresponding to individual cells at increasing distance from the irradiated one, as shown in the first frame of figure 3.1

data provide the first direct evidence that fPDT induce NO release from irradiated as well as non-irradiated cells, which may release ions, cytokines and other second messengers establishing a signalling intercellular network responsible for bystander effect in tumors.

Moreover these data support the notion that bystander cells actively participate in the spreading of the PDT response, as intracellular Ca^{2+} and NO production may be detected also at distant site from the target cell. The mechanism underpinning the crosstalk of this signalling network, however require further investigation. Thus, we have selected three parameters that characterize the observed signal patterns: the maximal concentration variation of Ca^{2+} and NO in bystander cells located in an annular region centred on the target cell -with an inner radius of 75μm and an outer radius of 120 μm- and the speed of Ca^{2+} wave computed by linear interpolation of time to half-maximum versus distance from target cell.

These data also provide a completely new insight in NO release modality during PDT. In fact, the shape of recorded NO signals in target cell, that show an extremely rapid concentration increase followed by an exponential decay, suggests a double mechanism in which, on one hand, NO is directly released from target cell and diffuse to bystander cells during the first seconds of photosensitization. Then, high NO levels in bystander cells are maintained even after central source depletion, suggesting NO enzymatic production in these cells. Moreover, fast NO release from target cell is in agreement with the reported capability of AlPc to buffer NO and the hypothesis of NO release during the PS oxidation, which might take place following photoactivation. Therefore, we could temporally distinguish two phases in PDT-induced NO signalling: a first one, lasting for few seconds in which diffusion dominated and a second one that is found to be primarily enzymatic dependent, as highlighted in figure 3.3.

NO production evoked by PDT raised the hypothesis that NO might be the product of NOS enzymes triggered by intracellular Ca^{2+} transients. Only constitutive eNOS and nNOS activity is considered CaM/Ca^{2+} dependent. However several reports demonstrated iNOS positivity in human tumor samples, including colon cancers.

Therefore we performed mRNA analysis to identify the NOS isoforms expressed by the C26GM cell line. We detected low absolute mRNA levels of all three isoforms (particularly low in the case of iNOS) and the highest signal corresponded eNOS.

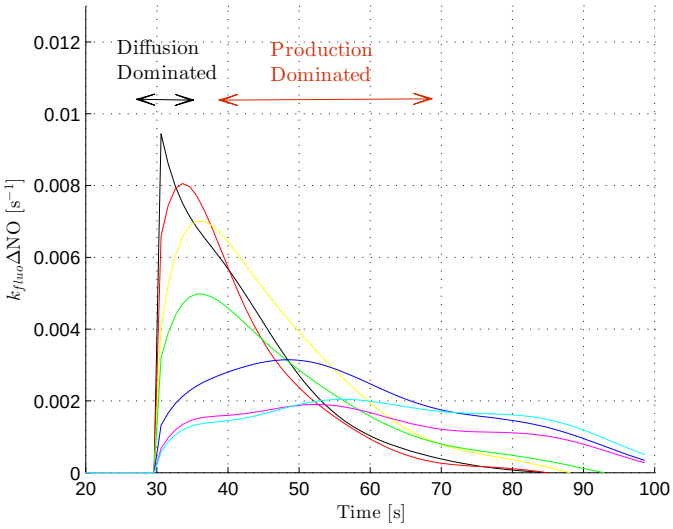

Figure 3.3: NO traces obtained within 7 regions of interest (ROIs) corresponding to individual cells at increasing distance from the irradiated one. PDT-induced NO signalling shows a two phases mechanism with a first diffusion dominated phase followed by a production dominated one.

3.1.2 Photodinamic Therapy and cell death

Both Ca^{2+} and NO are reported to be involved in the induction of apoptosis. Indeed, the loss of Ca^{2+} homeostasis may lead to cell injury as well as high levels of NO/RNS which, through modifications of death-related target proteins, mediate inhibition of cellular respiration, thus affecting mitochondrial membrane permeability, finally leading to cytochrome c release and initiation of apoptosis[53]. PDT has been indeed demonstrated to trigger both apoptosis and necrosis[75]. Thus, we performed fPDT with AlPc and we evaluated the expression of specific apoptotic markers. In particular, we used pSIVA, an annexin-based, polarity sensitive probe for the spatio-temporal or kinetic analysis of apoptosis [30]. In these experiments, we monitored only Ca^{2+} (with fura-2) and not NO due to the overlap between CuFl and Psiva fluorescence emission spectra. After fPDT, we added pSIVA and propidium iodide (PI) to the extracellular medium. Fluorescence images were acquired every 30 min (1 frame for pSIVA and 1 frame for PI). The irradiated cell displayed a clearly detectable pSIVA signal afters 30 min (data non shown). Within 1 hour following PDT, both pSIVA and PI signals were detected in the irradiated cell and its nearest neighbours; thereafter the signals propagated to more remotely located bystander cells(Figure 3.4). By 4 hours about 40% of cells in the field has at least entered apoptotic cell death. No toxic effects were observed in control experiment, in which the PS AlPC was loaded but not

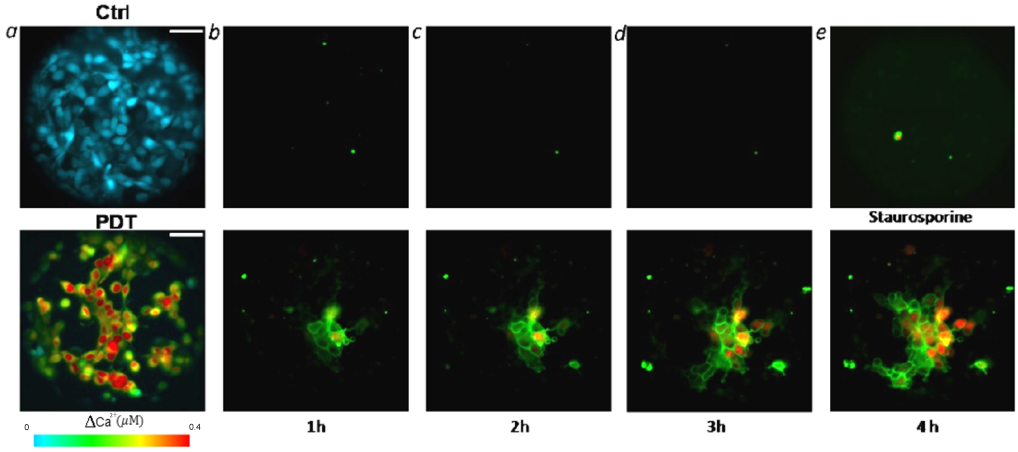

Figure 3.4: Photosensitization induces an "apoptotic death-wave". a. Representative false–color images of Fura-2 fluorescence ratio variation during fPDT in AlPC-treated C26GM cells either non-photostimulated (ctrl) or photosensitized (PDT). Ca^{2+} level variation is encoded as shown by the color scale bar. Time-lapse microscopy was used to monitor apoptosis by real-time detection of phosphatidylserine externalization in C26GM cells subjected or not to fPDT. Representative color-merged images of C26GM cells; propidium iodide fluorescence (red) and pSIVA fluorescence (green) at the indicated time (h, hours) following or not fPDT. As an apoptosis positive-control, cells were incubated with Staurosporine (e, upper image).Scale bars, 50 μm.

photoactivated. These data demonstrate that unless photostimulated, the PS is not able to trigger any Ca^{2+} wave. As internal positive control of the staining, control cells were treated with staurosporine, a well known apoptosis inducer(20 μM, 2 hour incubation) after 4 hours of recording (Figure3.4e). Altogether, these results support the notion that fPDT promotes bystander cell death and suggest that these effects may contribute significantly to the efficacy of PDT in cancer treatment.

3.1.3 Pharmacological interference experiments

In order to better characterize the temporal association among intracellular Ca^{2+} concentration variation and NO signals, we performed pharmacological interference experiments with different drugs modulating different key components of the Ca^{2+} signalling toolkit. Primarily, we performed the same fPDT experiments in Ca^{2+} free extracellular medium (supplemented with the Ca^{2+} chelator EGTA) to evaluate the relevance of Ca^{2+} influx from extracellular milieu; moreover, we exploited the phospholipase C inhibitor U73122 to reduce the amount of intracellular IP_3 and consequently Ca^{2+} release from the intracellular stores. Aiming at identifying the molecular mechanisms responsible for Ca^{2+} wave propagation we repeated fPDT experiments by blocking connexin based channels, both gap junctions and connexin hemichannels by the use of the specific inhibitors CBX, FFA and 2-APB [6]. Taken together these data suggest that IP_3 mediated Ca^{2+} release from intracellular stores is instrumental for the spreading of PDT response. Furthermore, gap junction channels play a key role in propagating PDT induced Ca^{2+} waves as well as NO signals in bystander cells.

Since ATP, which might be released by apoptotic cells through pannexin channels[33], thus activating purinergic receptors expressed on nearby cells surface, could promote Ca^{2+} wave propagation, we tested also the impact of pannexin blockage by Probenecid or aspecific purinergic receptors inhibition by Suramine in fPDT induced bystander signals.

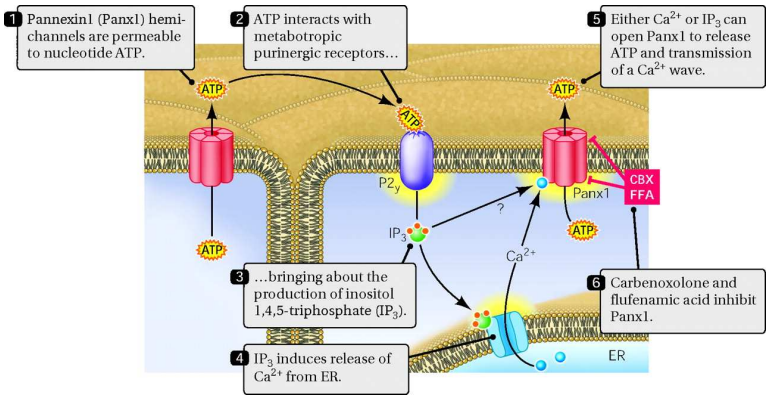

Figure 3.5: Role of pannexin hemichannels and purinergic receptors in the propagation of Ca^{2+} signals (reproduced from [8]). The released ATP would interact with metabotropic purinergic receptors (P2Y, blue), bringing about the production of the second messenger IP_3 (green circles), which induces Ca^{2+} release from the ER. Either IP_3 or a Ca^{2+}-dependent process would then trigger the opening of Panx1 hemichannels, ensuring the release of ATP and the transmission of a Ca^{2+} wave.

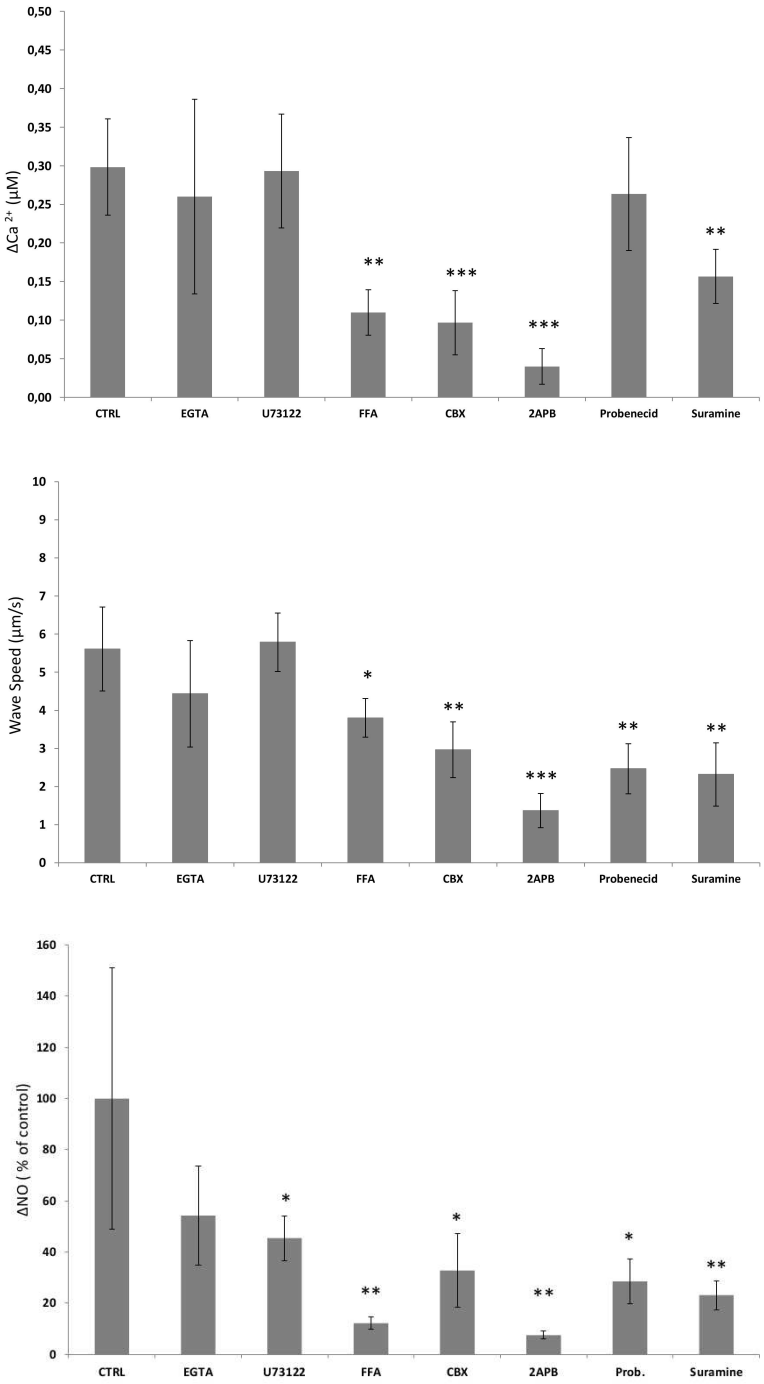

Figure 3.6: Pharmacological interference in fPDT experiments with different drugs (see methods for details). Maximal variation of Ca^{2+} concentration expressed in μM and NO levels, expressed as percentage of control average levels, (ΔCa^{2+} and ΔNO) were measured in 36 randomly selected cells between 75 μm and 120 μm from target cell. For each drug reported values represent an average on three independent experiments.

3.2 Mathematical model of Bystander Effects

As we have seen, fPDT induces Ca^{2+} transients and NO signals in neighbouring cells, spreading at great distances from target cell, taking account of bystander effect.

The task of this section is to develop a mathematical model of this signalling patterns capable of giving us a better comprehension of the molecular mechanisms underlying bystander effect in PDT, with particular reference to NO signals.

As we already stressed, the pattern of NO signal propagation shows a diffusive contribute from a central source and also a production contribution likely due to eNOS activation follows Ca^{2+} wave propagation. So we introduced a simple diffusive model in which NO is released from target cell and diffuse to bystander cells. As we are going to see, such approach allows to single out enzymatic production of NO. In order to describe the enzymatic contribution to NO signals we have developed a model, based on an extensive literature study, to quantitatively describe NO production by eNOS and eNOS activation by Ca^{2+} through CaM. Neither the enzymatic process catalysed by eNOS nor eNOS binding kinetics to CaM are completely clear so a few hypotheses are going to be introduced. Significative parameters, like enzyme activity and half maximal effective concentrations (EC_{50}) for Ca^{2+}, were also predicted and compared with reported values, in order to test the reliability of the model.

3.2.1 Diffusive Bystander Effects

Nitric Oxide chemistry and lifetime

The reaction chemistry of NO is complex due the instability of most of its reaction products. In particular, NO lifetime in a real tissue or simply in the presence of cells, is a complex matter because enzymatic process involving NO, protein nitrosation and NO localization in hydrophobic regions have significative effects. NO lifetime in physiological conditions spread from few milliseconds to few seconds depending on oxygen concentration and tissues properties[96].

In order to obtain a complete overview of possible biological effects of NO and the factors that influence its lifetime, is useful to systematically analyze its chemistry. The reaction pathways involving NO are complex for two reasons, the first one is that it is thermodynamically unstable, the second is that most of its oxides have an unstable electronic structure[32]. NO itself, in condition of high pressure and temperature, can directly dismutate via the pathways:

$$3\,NO \longrightarrow N_2O + NO_2 \tag{3.1}$$

$$2\,NO \longrightarrow N_2 + O_2 \tag{3.2}$$

NO can also be oxidized to the nitrosonium cation NO^+ through the reaction:

$$NO \longrightarrow NO^+ + e^- \tag{3.3}$$

Reaction potential of -1.21 V, needed for the oxidation, exceeds range of typical reaction potentials found *in vivo* so its production in biological context is probably due

to heterolytic fission of N_2O_4. Even when formed, nitrosonium has a short lifetime in water because, in physiolgical pH range, the reaction:

$$NO_2^- + 2\,H^+ \longleftrightarrow NO^+ + H_2O \tag{3.4}$$

is heavily shift to the left side[51]. Alternatively NO can be reduced to the nitroxyl anion NO^-, isoelectronic to O_2, that may exist in a spin triplet or singlet state as dioxygen. Triplet ground state $^3NO^-$ can be protonated to HNO and then irreversibly decomposed to N_2O .

At low concentration as in biological situation, the reactions 3.2 result inhibited but NO_2, that take on an important part in biological sample due to its role in generate nitrosating agents, may be formed by not yet clarified reactions with dioxygen for wich two different pathways has been proposed. Both pathways have a net balance

$$2\,NO + O_2 \longrightarrow 2\,NO_2 \tag{3.5}$$

After $2\,NO_2$ radical production the appearance of nitrostaing species like N_2O_4 and N_2O_3 occurs. These species are highly reactive and most important for biological system because together with NO^+ are the only compounds with proven ability of S-nitrosation[32]. The nitrosation reactions are fast processes that transform a thiol group RSH to a nitrosothiol RSNO

$$N_2O_4 + RSH \longrightarrow NO_3^- + RS\text{-}NO + H^+ \tag{3.6}$$
$$N_2O_3 + RSH \longrightarrow NO_2^- + RS\text{-}NO + H^+ \tag{3.7}$$

These nitrosation processes are so fast that dominate, at physiological thiol concentrations, even if in competition with hydrolysis to nitrite or nitrate, according to the reactions

$$N_2O_4 + H_{20} \longrightarrow NO_2^- + NO_3^- + 2\,H^+ \tag{3.8}$$
$$N_2O_3 + H_2O \longrightarrow 2\,NO_2^- + 2\,H^+ \tag{3.9}$$

The balance of above reactions produces nitrite with a third order reaction

$$\frac{d}{dt}[NO_2^-] = k[\cdot NO][O_2] \tag{3.10}$$

and a rate $k = 5 * 10^{-6}\ M^{-2}\ s^{-1}$[29]. The low rate of this reaction guarantees that uncatalyzed oxidation of NO through above reactions doesn't affect significantly NO lifetime. Even at full O_2 concentration of hundreds of μM, such value implies a lifetime of many hours in aqueous solution.

However is clear that in biological systems the situation is more complex, first of all the heterogeneous structure with regions of low polarity give raise to local higher concentration of NO significantly accelerating autooxidation up to 300-fold[61], furthermore, NO consumption by enzymatic pathways, such that involving oxyhemoproteins and superoxide, could also take place.

In fully oxygenated blood the dominant heme species is $\alpha(FeO_2)_2 - \beta(FeO_2)_2$ which rapidly oxidizes NO to nitrate with a high reaction rate of $k \sim 1 * 10^7$ M^{-1} s^{-1} and is the dominant NO loss in the vasculature in which NO lifetime can reach $\tau \sim 2$ ms[96].

A higher reaction rate applies to the reaction with superoxide radical, also produced during PDT, that produce peroxynitrite. This is a diffusion limited reaction with reported rates between $4.3 * 10^9$ to $1.9 * 10^{10}$ M^{-1} s^{-1}. Peroxynitrite is a powerful oxidizing agent and could be highly damaging to cellular processes reacting with the metal containing site of many enzymes. Hemoprotein in particular, like hemoglobine, cytochromes and NOSs, are prone to modification by peroxynitrite that inhibit their catalytic activity.

These studies show how complex NO chemistry is in biological system, with differences in NO consumption between intracellular and extracellular medium and also between different subcellular structures. In the absence of really detailed information about this environment a simpler description is needed. As shown by Lancaster et al, analysing NO consumption in a cells suspension, these complex reaction pathways can be efficiently approximated by a simpler kinetics law that relates NO loss to O_2 concentration and cell density:

$$\frac{d[\mathrm{NO}]}{dt} = -k_{obs}[\mathrm{O_2}][\mathrm{NO}][\mathrm{Cell}] \tag{3.11}$$

where [Cell] is numeric cells concentration and a value of $5.38 \pm 0.3 * 10^{-4}$ $M^{-1}s^{-1}$ (cell/ml $)^{-1}$ for k_{obs} for hepatocytes is reported [96].

Nitric Oxide diffusion

In order to describe the diffusive contribution to NO bystander signals, we consider a simple model in which NO buffered by AlPc and eventually heme-proteins, is release during photoactivation and diffuse to neighbouring bystander cells. A common assumption founded in literature is the ability of NO to freely diffuse across cell membranes due to its small molecular weight and neutral charge[65][38]. Such assumption allows to mediate the effects of reactions that take place in extracellular or intracellular milieu leading to a simplified description of NO chemistry, in which all previously described reactions are summarized by a single effective degradation constant k_{deg} that could depend on O_2 and cell concentrations. In such conditions NO concentration is determined by:

$$\frac{d[\mathrm{NO}](\mathbf{r},t)}{dt} = D_{\mathrm{NO}}\nabla^2[\mathrm{NO}](\mathbf{r},t) - k_{deg}[\mathrm{NO}](\mathbf{r},t) \tag{3.12}$$

where $D_{\mathrm{NO}} = 3300$ $\mu m^2 s^{-1}$ is the diffusion coefficient for NO.

Sucessive investigations pointed out that NO diffusion coefficient is highly reduced in lipophilic media, like biomembranes and lipoproteins[73] [62]. Accordingly to these facts, it was recently reported that cell membrane represents a significant diffusion barrier for NO transfer and diffusion through cell membranes requires specific connexin-based channels[109]. Following such model we need to distinguish between NO concentration in the extracellular space $[\mathrm{NO}]_{ex}$ and in the cytoplasm $[\mathrm{NO}]_{in}$. In the

extracellular space NO can freely diffuse and the degradation term could be neglected as follows from previously described NO reactions in water. Intracellular NO concentration is influenced by NO influx from connexin-based channels and a degradation term that summarize NO consumption by previously described processes. The flux of NO between extracellular and intracellular space was assumed to be proportional to the difference of NO concentration between them. Therefore $[\mathrm{NO}]_{ex}$ and $[\mathrm{NO}]_{in}$ are determined by:

$$\frac{d[\mathrm{NO}]_{ex}(\mathbf{r},t)}{dt} = D_{\mathrm{NO}}\nabla^2[\mathrm{NO}]_{ex}(\mathbf{r},t) + \sum_{j=1}^{N} k_{hc}\left([\mathrm{NO}]_{in,j} - \langle[\mathrm{NO}]_{ex}(\mathbf{r},t)\rangle_j\right) \tag{3.13}$$

$$\frac{d[\mathrm{NO}]_{in,j}}{dt} = k_{hc}\left(\langle[\mathrm{NO}]_{ex}(\mathbf{r},t)\rangle_j - [\mathrm{NO}]_{in,j}\right) - k_{deg,in}[\mathrm{NO}]_{in,j} \tag{3.14}$$

where $[\mathrm{NO}]_{in,j}$ is NO cytoplasm concentration for cell j, k_{hc} represents the hemichannel transfer rate that depends on the number of channels and their unitary permeability, $k_{deg,in}$ is the intracellular effective degradation constant and $\langle[\mathrm{NO}]_{ex}(\mathbf{r},t)\rangle_j$ represents NO extracellular concentration in proximity of cell j.

This model for NO diffusion is also supported by our experimental results: indeed the amplitude of NO signals in groups of bystander cells selected at fixed distances from the target cell, turn out to be heterogeneous. Such variability strengthens the hypothesis of connexin involvement in NO spread, because the hemichannel transfer rate depends on the variable number of channels expressed in every cell. Moreover, experiments carried out in our lab with the partially selective pannexin blocker Probenecid, shows a strong reduction in the amplitude of NO signals without decisively affect the amplitude of Ca^{2+} signals. This result suggests that hemichannels-blocking can prevent NO influx from extracellular space, confirming connexin channel role in NO trafficking.

Equations 3.13 and 3.14 were solved with a simple finite difference approach with a timestep $\Delta t = 50$ μs. The domain in which the equations were solved and the corresponding boundaries conditions are illustrated in figure 3.7. The domain volume was discretized with a step size of 10 μm in the z direction and 2 μm in the x and y directions. Cells were modelled as polygons reproducing experimental distribution located at $z = 0$ μm, while a reflecting boundary at $z = -10$ μm describe the effect of underlying glass. Finally, absorbing boundaries were considered at $z = 150$ μm and in correspondence of x and y limits at $+300$ μm and -300 μM. The algorithm was implemented with python, taking advantage of Scipy library and particularly sparse matrices modules[44].

Our algorithm was tested solving eq. 3.12 for different diffusion coefficient values because in such cases an analytical solution can be derived for a point source situated in the origin. The analytical solution of eq.3.12 with a reflecting boundary at z_b, for an impulsive initial condition in the origin $[\mathrm{NO}](\mathbf{r},t_0) = \delta(\mathbf{r})$ results:

$$[\mathrm{NO}](\mathbf{r},t) = \frac{1}{(4\pi D_{\mathrm{NO}}t)^{3/2}} e^{-\frac{x^2+y^2}{4D_{\mathrm{NO}}t}} e^{-kt}\left(e^{-\frac{z^2}{4D_{\mathrm{NO}}t}} + e^{-\frac{(z_b-z)^2}{4D_{\mathrm{NO}}t}}\right) \tag{3.15}$$

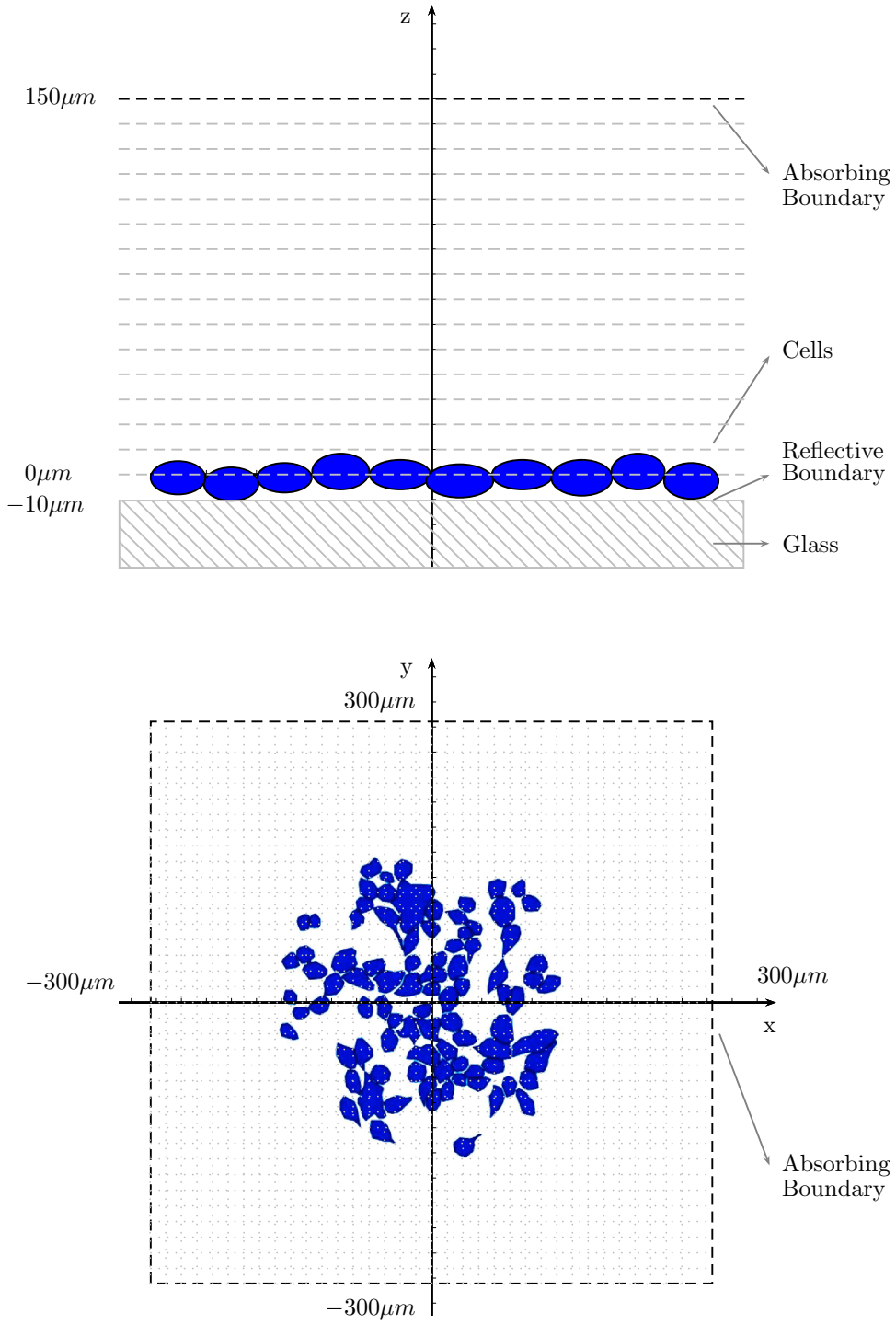

Figure 3.7: Scheme of model geometry and boundaries

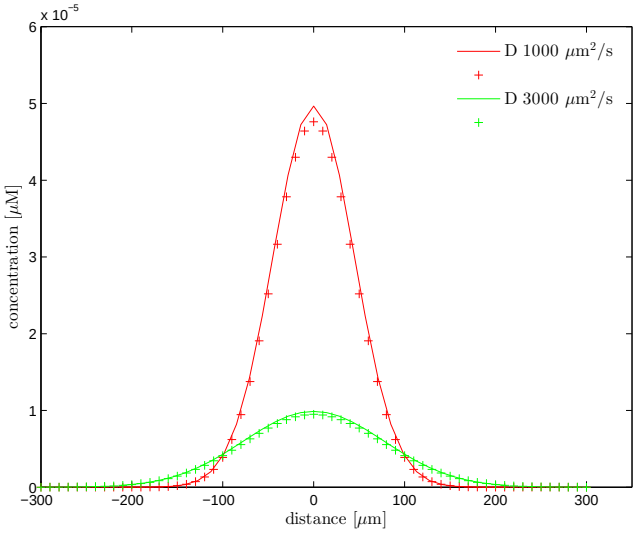

Figure 3.8: Analytical and numerical solution of eq.3.12 for an impulsive initial conditions in the origin, computed at $z = 0$.

The comparison of analytical and numerical solution of eq. 3.12 is show in figure 3.8.

Therefore eq. 3.13 and 3.14 were solved in order to reproduce the diffusive component of NO bystander signals. In such simulations, the measured NO concentration in target cell was used as an additional boundary condition for the model. Naturally, NO increase in bystander cells due to diffusion from the central source, depends on $k_{deg,in}$ and k_{hc}. For the first parameter, possible values ranges from 10 s^{-1} to less than 0.5 s^{-1}, corresponding to reported extravascular half-life of NO from 0.09 to > 2 s[96]. Like Ca^{2+} or IP_3 influx through gap junctions, transfer rate k_{hc} will be proportional to the number of channels and their unitary permeability, and inversely proportional to cell volume[39]. No values were reported in literature yet, so a wide range of k_{hc} values was tested.

Our results, illustrated in figure 3.9 highlight that NO level in bystander cells are weakly affected from parameter changes when k_{hc} exceed 5 s^{-1} or $k_{deg,in}$ is above 0.5 s^{-1}. Unfortunately we could not access the real values of those parameters, however in the aim of highlight the involvement of NO enzymatic production in fPDT we could consider threshold values in which the diffusive contribution to NO levels in bystander cells is maximum. Evaluating the differences between experimental values and predicted maximal diffusive contributions, give us a minimal estimate of the production term, its time-course and its amplitude relative to the central source. The resulting production components are shown in figure 3.10.

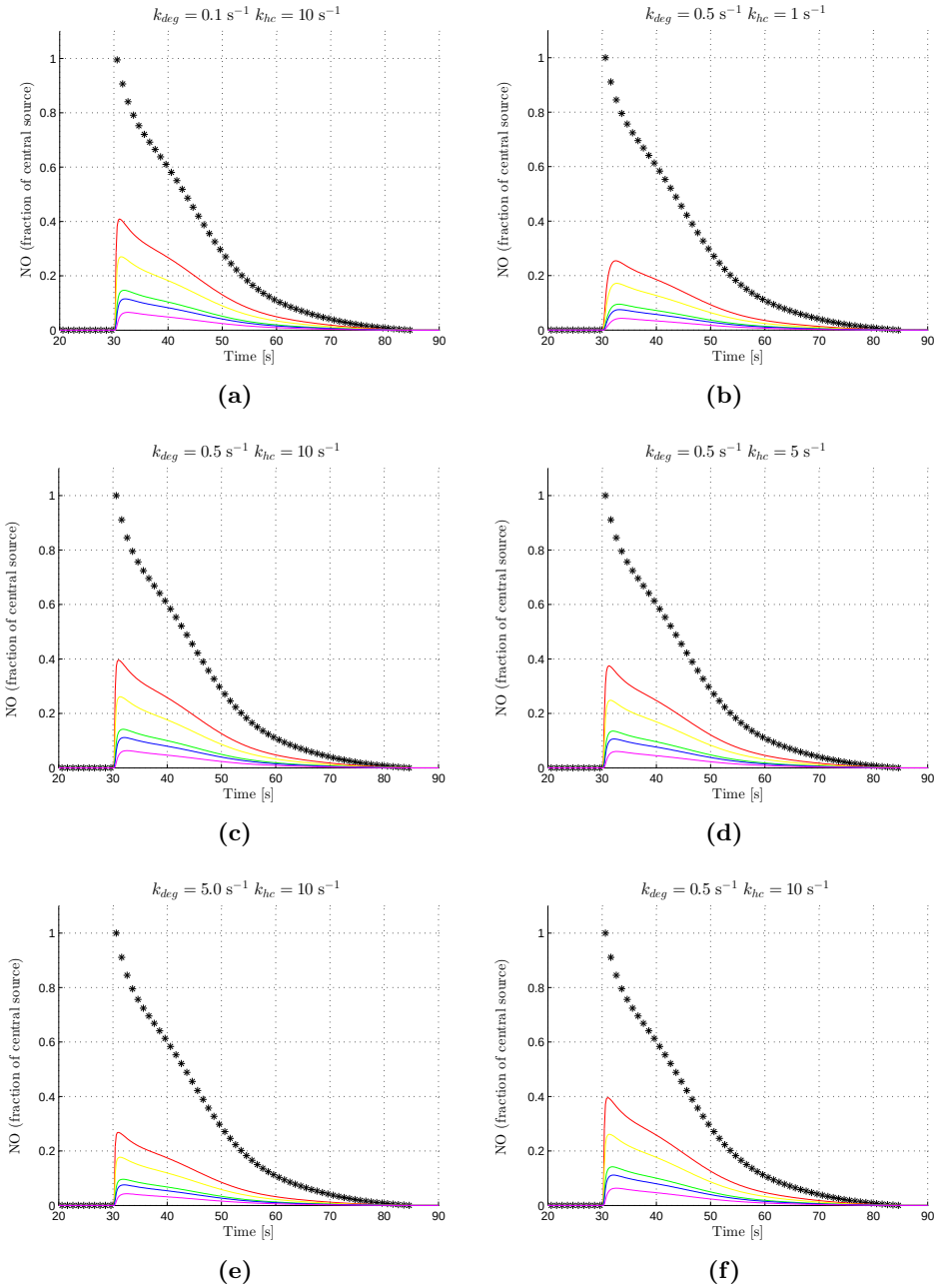

Figure 3.9: Simulations of NO levels in bystander cells, selected at increasing distance from the photoactivation spot, due to NO release from target cell (black data points), for different k_{hc} and $k_{deg,in}$ values.

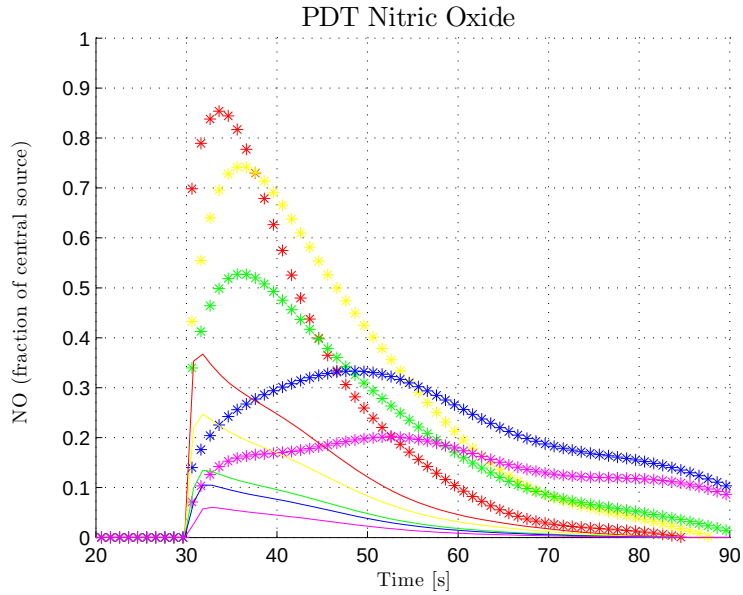

(a)

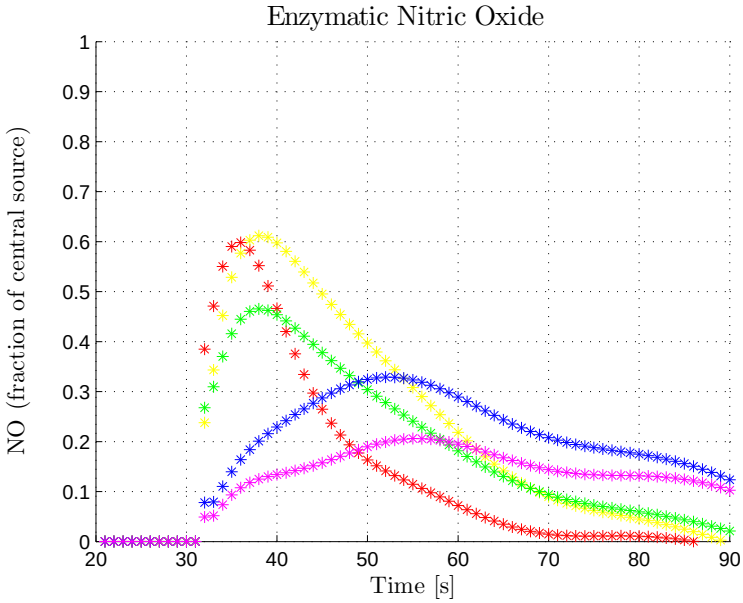

(b)

Figure 3.10: (a) NO signals evoked by fPDT whitin 5 ROIs at increasing distance from target cell, compared with the diffusive components due to NO release from target cell. (b) NO production components of PDT-evoked NO signals, obtained as the differences between experimental data and NO levels predicted from simulation. $k_{hc} = 5\ \mathrm{s}^{-1}$ and $k_{deg,in} = 0.5\ \mathrm{s}^{-1}$.

3.2.2 Enzymatic Nitric Oxide production

Nitric Oxide production rate

The biochemical pathway of NO production by NOS is a well studied enzymatic process but the precise description of the NOS molecular mechanism is still lacking. Consequently several models of NO production from NOS have been proposed in the last years and all of them share a similar overall reaction scheme but differ in the number, origin and characteristics of the electron transfer processes that take place during enzyme activity[88].

Global catalytic mechanism of NOS consists in two successive steps of oxidation that collectively need one molecule of L-Arg, two molecules of O_2, and three electrons. In the first step hydroxylation of L-Arg to NOHA takes place. In the second step NOHA acts as a substrate and is oxidized to L-Cit finally leading to the release of one molecule of NO and two molecules of water. With reference to the global mechanism illustrated in figure 3.11, the reaction starts with the oxidation of NADPH, that provide an electron through the NOS flavoprotein domain to ferric heme, reducing it to the ferrous form. This is the slowest step of the biosynthetic reaction and leads to the formation of ferric superoxide after O_2 binding[105]. The tetrahydrobiopterin (H_4B) reduction is the second slowest step of the process but is sufficiently fast to prevent superoxide release from ferrous heme group[21]. This step is one of the unique functional features of NOS because of the redox role of H_4B [88]. Another unique feature of

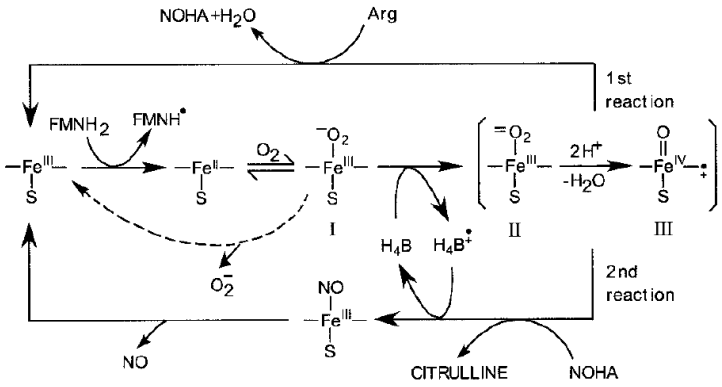

Figure 3.11: NO synthase global mechanism.[95]

this enzyme is its ability to achieve two different oxidative chemistries using the same constrained active sites, effectively after the reduction of ferrous superoxide to ferric oxide, the last one is rapidly protonated to form a heme iron-oxo species that may react directly with L-Arg or NOHA[81]. Reaction with NOHA produce a ferric heme NO complex($Fe^{3+}NO$) that only later dissociates releasing free NO[105]. Meanwhile $Fe^{3+}NO$ can be reduced to $Fe^{2+}NO$ which release NO very slowly and is instead oxidized by O_2 to nitrate (NO_3^-), moreover NO can also bind to NOS in both its ferric or ferrous oxidation states [90]. Consequently, after $Fe^{3+}NO$ biosynthesis is completed two different cycles compete: direct NO release could be considered part of a "productive cycle" whether reduction of $Fe^{3+}NO$ guides the enzyme into a "futile cycle"

Table 3.1: Concentration of coenzymes and substrates required to reach 50% of NO production and physiological concentration in different cell types. † The intracellular concentration of L-Arg has been reported to be ∼100 μM in endothelial cells. However the L-Arg availability to the enzyme is really lower due to the phenomenon known as the "L-Arg paradox" probably produced by the division of L-Arg in different pools or compartments[26][102].

	EC_{50}		Ref.	Range		Ref.
CaM	$0.008 - 0.009$	μM	[60] [34]	2-25	μM	[86] [14]
H_4B	$0.05 - 0.22$	μM	[60] [34] [78]	∼3.6	μM	[70]
NADPH	1	μM	[34]	∼166	μM	[70]
L-Arg	$0.9 - 2.9$	μM	[34] [107]	∼1-100	μM †	[107]
O_2	7.7	μM	[84]	50-170	μM	[98]

that at last produce nitrate instead of NO. Because of this mechanism the fraction of enzyme occupied with futile cycle depends on NO concentration, introducing a negative feedback mechanism that can modulate enzyme activity. As previously shown, the rate limiting step in NO synthesis is the reduction of ferric heme domain,which is considerably slower than that of other flavoheme enzymes similar to NOS. This peculiarity has a precise biological reason because increasing the reduction rate will partition more NOS in the futile cycle and ultimately convert the enzyme in a NO oxygenase[95]. Moreover, reaction rates are not the same for different NOS types, so futile cycle and NO feedback mechanism could have different roles. Particularly, eNOS is less sensitive to futile cycle mechanism [89].

In order to employ a Ca^{2+} to NO transduction model we have assumed the detailed NO biosynthesis scheme proposed by Chen and Popel[23] described in figure 3.12. The half maximal effective concentrations (EC_{50}) for substrates and cofactors have been reported by a variety of laboratories. A comparison between those values and physiological concentration ranges in different cells is reported in table 3.1. Notably typical intracellular concentration of H_4B and NADPH are far larger than those required to reach 50% catalytic activity. In order to simplify as much as possible our model, we assumed that all coenzymes and NADPH were present in excess and ignored their effects on the reaction pathway. Moreover we have included the binding kinetics of O_2 and L-Arg but we have considered their consumption negligible or completely balanced by external supply.

NO production mechanism shown in figure 3.12 was translated in a set of coupled differential equations reported in appendix A, describing concentration of different eNOS states, represented by the oxidation state of their heme group, and different substrates and products.

Kinetic parameters of the model were found in literature and are listed in table 3.2. The experimental values were measured in vitro under various temperature, often lower than in physiological condition. For this reason experimental measurements were

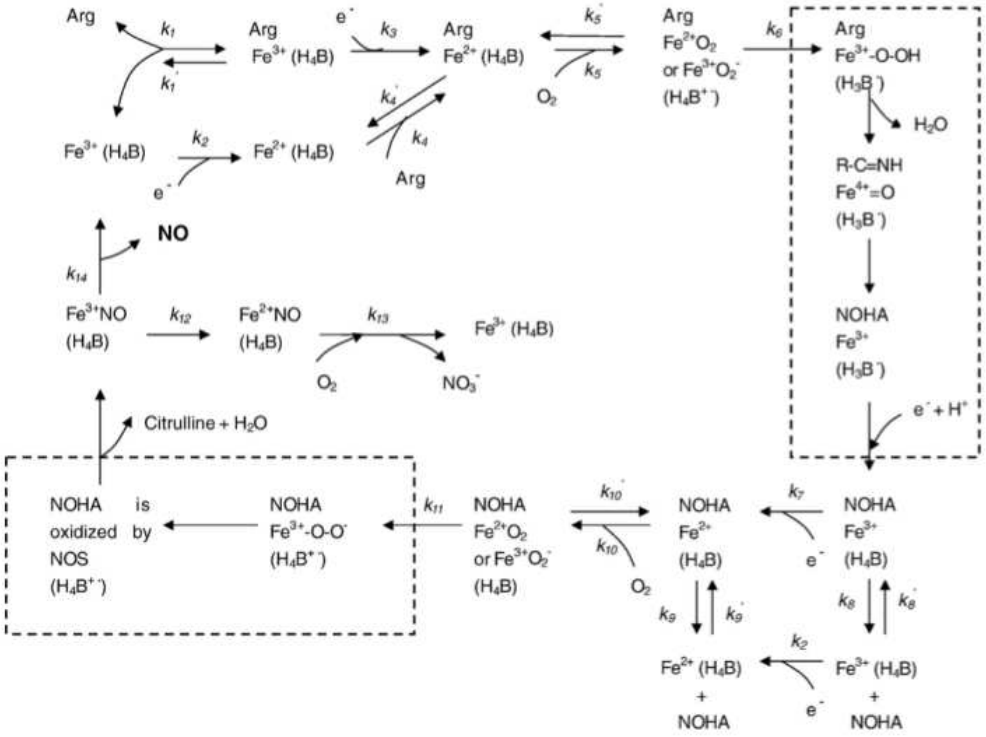

Figure 3.12: NO synthase detailed mechanism, different eNOS states are labelled with the oxidation state of their heme group. Reactions in boxes were considered fast and described as single reactions[23].

scaled through Arrhenius equation to extrapolate the values at 37°C.

$$k_{T_2} = k_{T_1} e^{-E_a \frac{T_1 - T2}{R T_1 T_2}} \tag{3.16}$$

where k_{T_1} and k_{T_2} are kinetic parameters at T_1 and T_2, R is the gas constant and E_a the activation energy of the process. Activation energies are not known for these processes, however several parameters have been measured at multiple temperatures, allowing to estimate their activation energy and scale up kinetic parameters.

For those parameters measured only at one temperature some assumptions are needed. As proposed by Chen and Popel[23], we have assumed that activation energy of those steps when NOHA was bound to eNOS were the same as for the corresponding steps when L-Arg is bound. Finally for ferric heme reduction, NO binding to ferric heme and $Fe^{3+}NO$ oxidation, the activation energies were assumed to be the average of all the available activation energies. We will refer to the activation energy of such processes as $E_{a,r}$ Side effects of this approximation were tested exploring the sensitivity of the model to this parameter. However, it was reported that NO production rate

Table 3.2: Kinetic parameters for eNOS, experimental values, predicted activation energies and predicted parameter values at 37°C. Activation energies indicated by † were extrapolated by similarities with other reaction steps whether values indicated by ⊙ were assumed to be the average of all available activation energies. See text for details.

Parameter	Values	Ref.	Value at 37°C	Unit	$E_a[J/mol]$
k_1	0.2(4°C) − 0.8(23°C)	[10]	1.99	$\mu M^{-1}s^{-1}$	$4.97 * 10^4$
k_1'	0.08(4°C) − 1.6(23°C)	[10]	11.50	s^{-1}	$1.07 * 10^5$
k_2	0.11(10°C)	[89]	1.01	s^{-1}	$6 * 10^4\odot$
k_3	0.11(10°C)	[89]	1.01	s^{-1}	$6 * 10^4\odot$
k_4	0.2(4°C) − 0.8(23°C)	[10]	$\mu M^{-1}s^{-1}$	1.99	$4.97 * 10^4$
k_4'	0.08(4°C) − 1.6(23°C)	[10]	11.50	s^{-1}	$1.07 * 10^5$
k_5	0.265(7°C) − 0.34(10°C)	[1][66]	2.58	$\mu M^{-1}s^{-1}$	$5.47 * 10^4$
k_5'	24(7°C) − 28(10°C)	[1][66]	98.03	s^{-1}	$3.38 * 10^4$
k_6	6.2(7°C) − 6.7(10°C)	[22][66]	12.59	s^{-1}	$1.70 * 10^4$
k_7	0.11(10°C)	[89]	1.01	s^{-1}	$6 * 10^4\odot$
k_8	0.8(23°C)	[36][10]	1.99	s^{-1}	$4.97 * 10^4\dagger$
k_8'	1.6(23°C)	[36] [10]	11.50	$\mu M^{-1}s^{-1}$	$1.07 * 10^5\dagger$
k_9	0.8(23°C)	[36] [10]	1.99	s^{-1}	$4.97 * 10^4\dagger$
k_9'	1.6(23°C)	[36][10]	11.50	$\mu M^{-1}s^{-1}$	$1.07 * 10^5\dagger$
k_{10}	0.26(10°C)	[1]	3.33	$\mu M^{-1}s^{-1}$	$5.47 * 10^4\dagger$
k_{10}'	18(10°C)	[89]	89.86	s^{-1}	$3.38 * 10^4\dagger$
k_{11}	14.5(7°C)	[66]	29.43	s^{-1}	$1.7 * 10^4\dagger$
k_{12}	0.11(10°C)	[89]	1.01	s^{-1}	$6 * 10^4\odot$
k_{13}	0.00429(10°C)	[89]	0.04	$\mu M^{-1}s^{-1}$	$6 * 10^4\odot$
k_{14}	2.5(4°C) − 3.5(23°C)	[89][66]	53.94	s^{-1}	$7.39 * 10^4$

is negligibly affected when a single kinetic parameter is altered, with the exception of the heme reduction rate[23].

We have used such model to predict the rate of NO production in a wide range of conditions in order to study the sensitivity of NO production to the availability of O_2 and L-Arg and to temperature changes also. Model equations were solved using a commercial software package (MATLAB 8.1, The MathWorks Inc., Natick, MA, 2013) and the Matlab ODE suite. The initial conditions were set such that all eNOS was in the ferric form, and L-Arg was not yet bound to eNOS. As shown in figure 3.13 (a) NO production reaches steady state in a few seconds. Enzyme concentration in different cells could range from 0.001 to 0.01 μM [5][64]. In such interval, and also at higher levels, NO production increased linearly with eNOS concentration as shown in figure 3.13 (b). Thus an increase in enzyme concentration can greatly improve NO production.

NO production rate increases rapidly with O_2 and available L-Arg concentrations until concentrations reach $\sim$ 5 μM and $\sim$ 10 μM respectively. Dependence of NO production rate from O_2 and L-Arg concentrations was explored in a large range of values from 1 μM to 200 μM O_2 and from 0.1 μM to 20 μM L-Arg at 25°C and 37°C, typical temperatures of *in vitro* and *in vivo* experiments respectively.

Moreover, in order to compare our rate predictions with experimental results, we have extrapolated from simulated data eNOS apparent activity $\mathcal{A}$, that is maximum

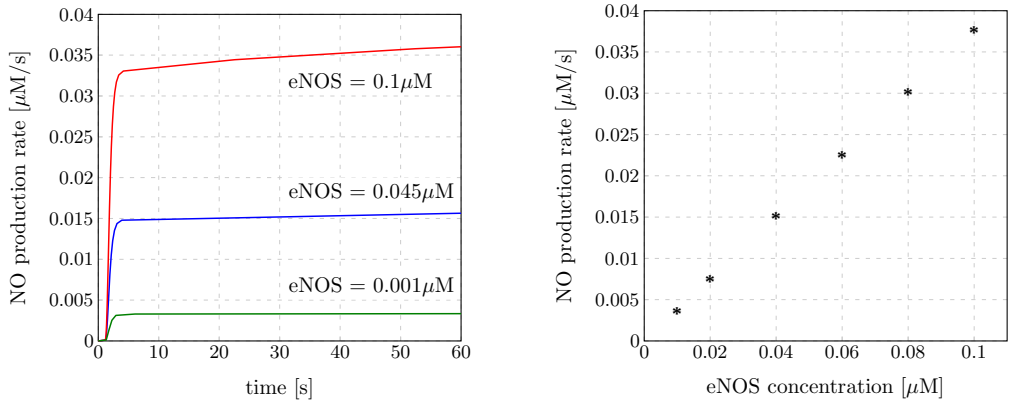

(a) **(b)**

Figure 3.13: (a) NO production rate at 0.01, 0.05 and 0.1 μM eNOS concentration. (b) Production rate at steady state linearly depends on eNOS concentration even at relatively high enzyme concentration. Such results eventually allow to use a simplified Michaelis Menten description also for high enzyme concentration. In both cases parameters value are: $T = 37°$C, Arg= 10 μM and $O_2 = 100$ μM

NO production rate per enzyme unit, by means of a simple double substrate enzyme model:

$$\text{eNOS+Arg} \rightleftharpoons \text{eNOS-Arg} + O_2 \rightleftharpoons \text{eNOS-Arg-}O_2 \longrightarrow \text{eNOS+NO}$$

Figure 3.14: Simple double substrates enzyme model with sequential binding.

Under usual Michaelis-Menten hypothesis, such as fast substrates equilibrium and low enzyme concentration ($[E] < [S_1], [S_2]$), this simplified model predicts a rate of NO biosynthesis at steady state of:

$$R_{NO} = \frac{\mathcal{A}[\text{eNOS}]_0}{1 + \frac{A}{[\text{Arg}][O_2]} + \frac{B}{[\text{Arg}]} + \frac{C}{[O_2]}} \tag{3.17}$$

where A, B, C and $\mathcal{A}$ depend on kinetic constants of the process and $[\text{eNOS}]_0$ is total enzyme concentration. Those parameters were evaluated by Least-Squares fit of data obtained from the complete model. Residual analysis shows that the simplified kinetics prediction does not precisely match data from complete model particularly at $T = 25°$C, condition in which the great majority of our *in vitro* experiments were carried on. First the hypothesis that the main contribution to this gap came from the availability of the inactive enzyme state was explored. The inactive enzyme fraction

at steady state was monitored over the same range of parameters and obtained values were always lower than 0.003. Also removal of inactive state from complete model did not produce appreciable changes in NO production rates so we rejected the hypothesis. Probably the non Michaelis Menten kinetics of the process emerge from the particular double cycle structure of the process. The scheme is also complicated by one irreversible step that occurs during NOHA synthesis, making impossible the application of systematic analysis of the whole process by means of King diagrammatic theory or later developments[49]. We have therefore empirically modified NO production expression from Michaelis Menten introducing higher order dependence on O_2 concentration in order to obtain a more detailed description of NO production and therefore a better estimates of enzyme activity:

$$R_{NO} = \frac{\mathcal{A}[\mathrm{eNOS_0}]}{1 + \frac{A}{[\mathrm{Arg}][\mathrm{O_2}]} + \frac{B}{[\mathrm{Arg}]} + \frac{C}{[\mathrm{O_2}]} + \frac{D}{[\mathrm{O_2}]^2}} \tag{3.18}$$

where the parameter D was introduced. Least-Squares interpolation of the data is shown in figure 3.16 and obtained parameters values are presented in table 3.3. Apparent eNOS activity obtained at 25°C and 37°C were 0.19 s^{-1} and 0.48 s^{-1} re-

Table 3.3: eNOS apparent activity and parameters values for the empirically corrected Michaelis Menten production kinetics.

	$T = 37\mathrm{C}^\circ$	$T = 25°\mathrm{C}$	Units
$\mathcal{A}$	0.48	0.19	s^{-1}
A	8.6	1.6	μM^2
B	0.17	0.28	μM
C	6.7	4.9	μM
D	-4.5	-2.7	μM^2

spectively and are consistent with values reported by several groups for purified eNOS, ranging from 0.04 s^{-1} [101] to 1.3 s^{-1} [60].

The activity of the enzyme is also a good parameter to evaluate the sensitivity of the model to the unknown activation energy $E_{a,r}$ that we have assumed to be the average of all available activation energies. Figure 3.15 shows eNOS activity computed for a wide range of $E_{a,r}$. Extreme values reported in literature for enzyme activity are also highlighted. Enzyme activity is strongly affected by changes in this parameter for which we could estimate a range of acceptable values between 2 kJ/mol and 100 kJ/mol.

Finally, we explored the NO production rate dependence from temperature in a physiologically relevant range. Predicted rates increase from 0.005μM s^{-1} to 0.03μM s^{-1} with a temperature increase from 15°C to 40°C.

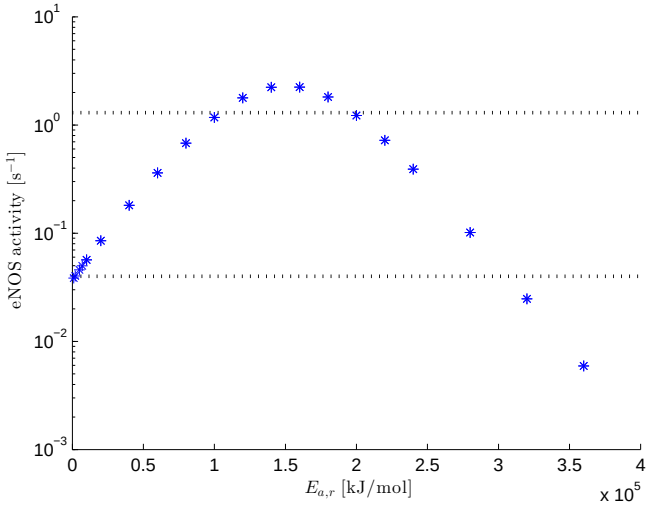

Figure 3.15: eNOS activity computed for a wide range of $E_{a,r}$ values. Horizontal lines highlight the range of activity values reported in literature.

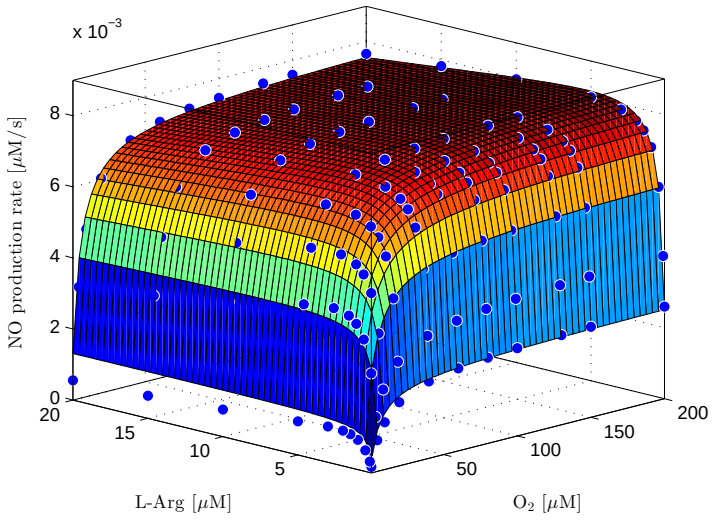

Figure 3.16: NO production at steady state predicted from complete model at $T = 25$°C and interpolated with equation 3.18.

.

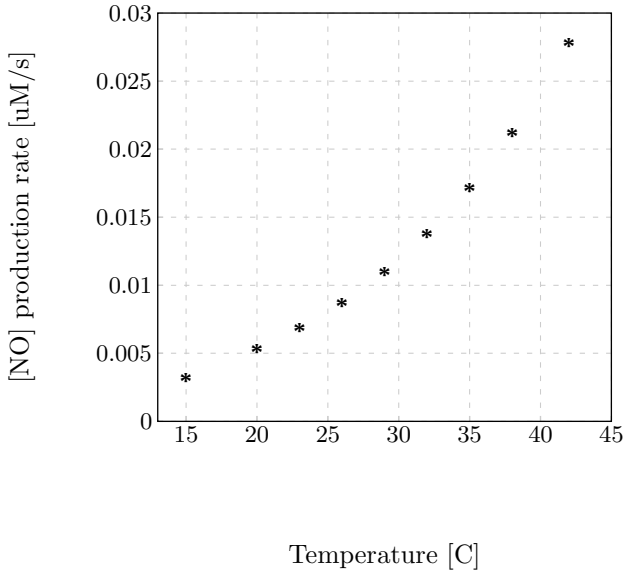

Figure 3.17: NO production at steady state predicted from complete model at various temperatures. Other parameters were set at typical physiological values [Arg] = 3 μM, [O_2] = 100 μM and [eNOS] = 0.045 μM .

NOS activation

Ca^{2+}-dependent activation of eNOS and nNOS is mediated by the ubiquitous Ca^{2+} binding protein CaM. CaM is formed by two lobes that contain two E-F hands each one capable of binding two Ca^{2+} ions in a cooperative way, providing on the whole four Ca^{2+} binding sites. Importantly nNOS and eNOS can be activated only by fully saturated CaM due to regulatory elements that characterize enzyme structure.

A key element of Ca^{2+} to NO transduction mechanism is therefore Ca^{2+} binding to CaM. This process takes place independently at the N- and C-terminus of CaM where two Ca^{2+} ions bind to the protein with different cooperative kinetics. Due to the fact that each one of the four Ca^{2+} binding sites could be in a bound or unbound state, a complete description of the system needs 16 independent variables. Since we are only interested in saturated CaM concentration and different sites of the same terminal are indistinguishable before the first ion is bound, we can consistently develop a simplified description that only needs nine independent variables. We labelled each CaM state in our model with the number of Ca^{2+} ions bound to N or C terminal and considered all possible reactions. The resulting reactions network is shown in figure 3.18 whereas detailed reactions at C and N terminal are shown in figure 3.19.

Figure 3.18: Ca^{2+}-CaM binding scheme.

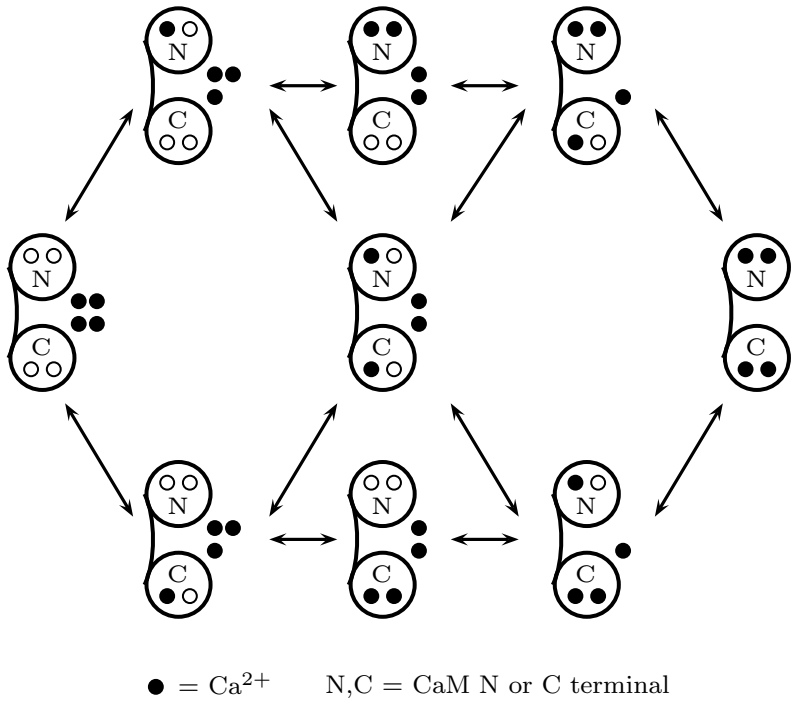

Figure 3.19: Cooperative Ca^{2+} binding kinetics to CaM at N and C terminal. Factors 2 on reaction rates were introduced considering indistinguishable different binding sites situated at the same CaM terminal.

N-terminal reactions:

$$\mathrm{CaM}+2\mathrm{Ca}^{2+} \underset{k'_{\mathrm{N1}}}{\overset{2*k_{\mathrm{N1}}}{\rightleftharpoons}} \mathrm{CaM(Ca)_{1N}}+\mathrm{Ca}^{2+} \underset{2*k'_{\mathrm{N2}}}{\overset{k_{\mathrm{N2}}}{\rightleftharpoons}} \mathrm{CaM(Ca)_{2N}}$$

k_{C2}

C-terminal reactions:

$$\mathrm{CaM}+2\mathrm{Ca}^{2+} \underset{k'_{\mathrm{C1}}}{\overset{2*k_{\mathrm{C1}}}{\rightleftharpoons}} \mathrm{CaM(Ca)_{1C}}+\mathrm{Ca}^{2+} \underset{2*k'_{\mathrm{C2}}}{\rightleftharpoons} \mathrm{CaM(Ca)_{2C}}$$

Table 3.4: Kinetics parameters of Ca^{2+} binding to CaM[31].

k_{N1}	$7.9*10^8$	$\mathrm{M^{-1}s^{-1}}$
k'_{N1}	$1.6*10^5$	$\mathrm{s^{-1}}$
k_{N2}	$3.2*10^10$	$\mathrm{M^{-1}s^{-1}}$
k'_{N2}	$2.0*10^4$	$\mathrm{s^{-1}}$
k_{C1}	$7.9*10^7$	$\mathrm{M^{-1}s^{-1}}$
k'_{C1}	$2.5*10^3$	$\mathrm{s^{-1}}$
k_{C2}	$2.5*10^7$	$\mathrm{M^{-1}s^{-1}}$
k'_{C2}	15.8	$\mathrm{s^{-1}}$

Rate constants of the process were recently measured monitoring Ca^{2+} dynamics after rapid flash photolysis of caged Ca^{2+} in presence of CaM mutants. Resulting parameters are shown in table 3.4 and characterize CaM as the fastest Ca^{2+} binding proteins. As first suggested by Faas et al.[31], when intracellular Ca^{2+} increases, it is rapidly buffered by CaM on a μs timescale and is then redistributed to slower but more stable CaB. In details, simulation conducted starting from these data, showed that within 40 μs after Ca^{2+} influx almost 80% of intracellular Ca^{2+} increase is bound to CaM N-lobe. Later, after a few milliseconds, Ca^{2+} is redistributed between C-lobe and other CaB. The overall mechanism is based on sequential binding events in which Ca^{2+} is first caught by the fast but low affinity buffer CaM and then transferred to a slow but high-affinity buffer.

CaM fast buffer mechanism is also influenced by CaM target proteins. Effectively when Ca^{2+} saturated CaM is bound to eNOS, Ca^{2+} dissociation rate from CaM results modified as we are going to see. In general, activation of CaM target proteins follow the reaction scheme illustrated in figure 3.21. With reference to eNOS, we have previously seen that CaM can bind the enzyme only when is Ca^{2+} saturated, whether CaM dissociation takes place in two distinct phases: as reported by A. Persechini et al., when

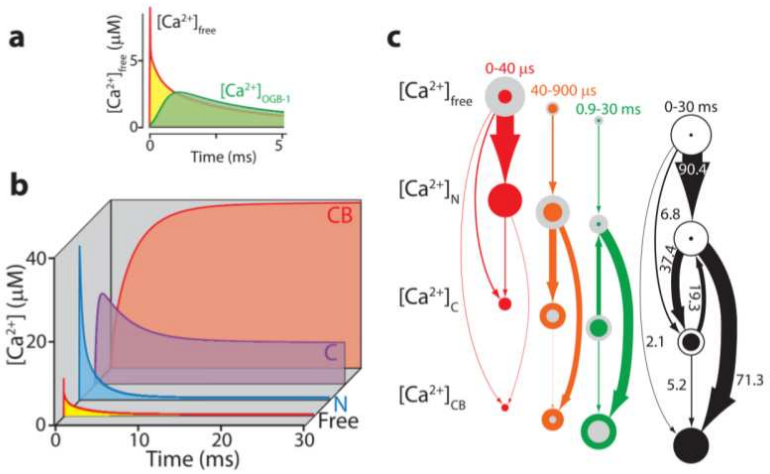

Figure 3.20: Ca^{2+} distribution in CaM N-lobe, C-lobe and other Ca^{2+} buffers on μs timescale. (Reproduced from [31]).

.

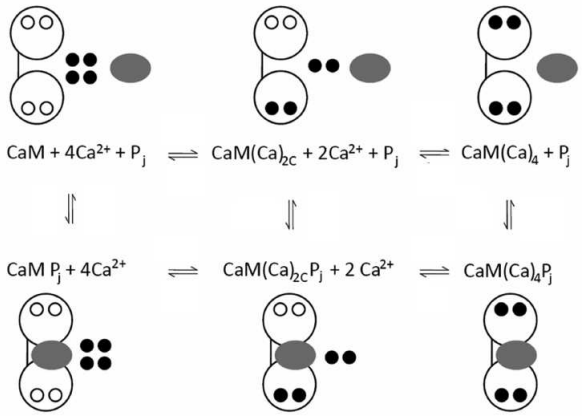

Figure 3.21: General network of CaM reactions with target enzymes. (Reproduced from[92]).

.

CaM is bound to eNOS, Ca^{2+} dissociation takes place more rapidly at the N-terminal resulting in enzyme inactivation. At a later stage release of Ca^{2+} from C-terminal take place and the NOSCaM complex dissociates[79].

Recently Salerno at al. has reported the first detailed measurements of eNOS and nNOS dissociation rates from CaM. Consistently with the presented reaction scheme they have found two distinct dissociation rates in condition of high or zero Ca^{2+} concentration and a transition point between different rates at $[Ca^{2+}] \simeq 300$ nM[68]. We have interpreted these data in the context of the model 3.21, simplifying it as much as possible in order to achieve the minimal model that can account for exclusively activation by saturated CaM and reported double phases dissociation mechanism. We have considered two distinct enzyme states, labelled NOSCaM and NOSCaM*. The

first one corresponds to the active form of the complex where CaM is Ca^{2+} saturated whether NOSCaM* corresponds to inactive state in which Ca^{2+} release from N-lobe has taken place and enzyme activity is blocked. Dissociation of the complex could take place both by the active and inactive form. The resulting model is shown in figure 3.22 where k_{NOS_1} and k_{NOS_2} are NOSCaM formation and dissociation rates for the active form of the complex, $k_{\mathrm{NOS}_{eq}}$ is the equilibrium constant between active and inactive states and k_{NOS_d} is the dissociation rate of the inactive state.

Figure 3.22: NOS activation model

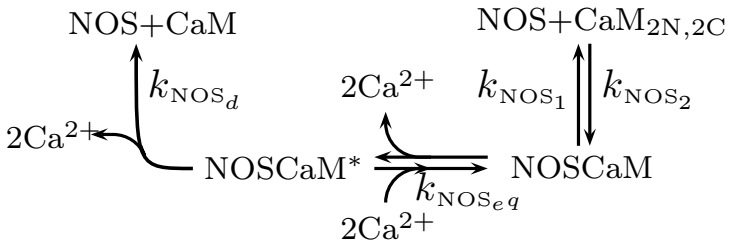

In absence of more detailed information we considered the transition between active and inactive state at instantaneous equilibrium. Hence fraction of the complex in the inactive state results Ca^{2+} dependent as follow:

$$\frac{[\mathrm{NOSCaM}^*]}{[\mathrm{NOSCaM}^*] + [\mathrm{NOSCaM}]} = \frac{1}{1 + [\mathrm{Ca}^{2+}] * k_{\mathrm{NOS}_{eq}}} \tag{3.19}$$

Kinetic parameters of our model were extrapolated from experimental data reported in [68]. At high Ca^{2+} concentration the complex accumulates in the active state therefore we have set dissociation rate from active state k_{NOS_1} to that reported to be 0.02 s^{-1} at high Ca^{2+} levels. When Ca^{2+} concentration approaches zero the equilibrium is heavily shifted to the inactivated form so we have considered dissociation rate k_{NOS_d} equal to that reported in presence of the Ca^{2+} chelator EDTA equal to $0.22s^{-1}$[68] The dissociation rate results slow at high Ca^{2+} level but between 300 nM to 30 nM increase rapidly reaching value found in EDTA. Thus, to determine equilibrium rate k_{eq}, we have considered that at 300 nM $[Ca^{2+}]$ only 10% of the complex is present in the inactive state whether at lower concentration the equilibrium is fast shifted to inactive form. The resulting k_{eq} was found to be 100 μM^{-2}.

Finally, we need to extrapolate from experimental data the NOSCaM complex formation rate. In order to estimate this parameter we considered reported measurements of eNOS binding to CaM at saturating Ca^{2+} concentrations ($[Ca^{2+}] = 10$ μM) and constant eNOS concentration of 10 nM that results in a pseudo first order rate of NOSCaM formation of $0.05s^{-1}$[31]. In such conditions NOSCaM concentration follows:

$$[\mathrm{NOSCaM}](t) = [\mathrm{CaM}]_0 \frac{[\mathrm{NOS}](1 - e^{-([\mathrm{NOS}]k_{\mathrm{NOS}_2} + k_{\mathrm{NOS}_1})t})k_{\mathrm{NOS}_2}}{[\mathrm{NOS}]k_{\mathrm{NOS}_2} + k_{\mathrm{NOS}_1}} \tag{3.20}$$

where ([NOS]$k_{NOS_2} + k_{NOS_1}$) corresponds to the pseudo first order rate of the process. The resulting NOSCaM formation rate is k_{NOS_2} =4.8 $\mu\mathrm{M}^{-1}$ s^{-1}.

The developed eNOS activation network was then coupled with previously described NO production model. To couple those models we have assumed that every state during NO synthesis could be put in a inactivated state when Ca^{2+} unbinds from CaM N-lobe. Moreover we have considered that inactivated enzyme units could be restored in their original state if Ca^{2+} binding takes place. The resulting model is shown in figure 3.23.

Figure 3.23: Coupling of eNOS activation model to NO biosynthesis model. Every state of the enzyme, labelled with the oxidative state of corresponding heme group, was doubled with the addition of the corresponding inactive state.

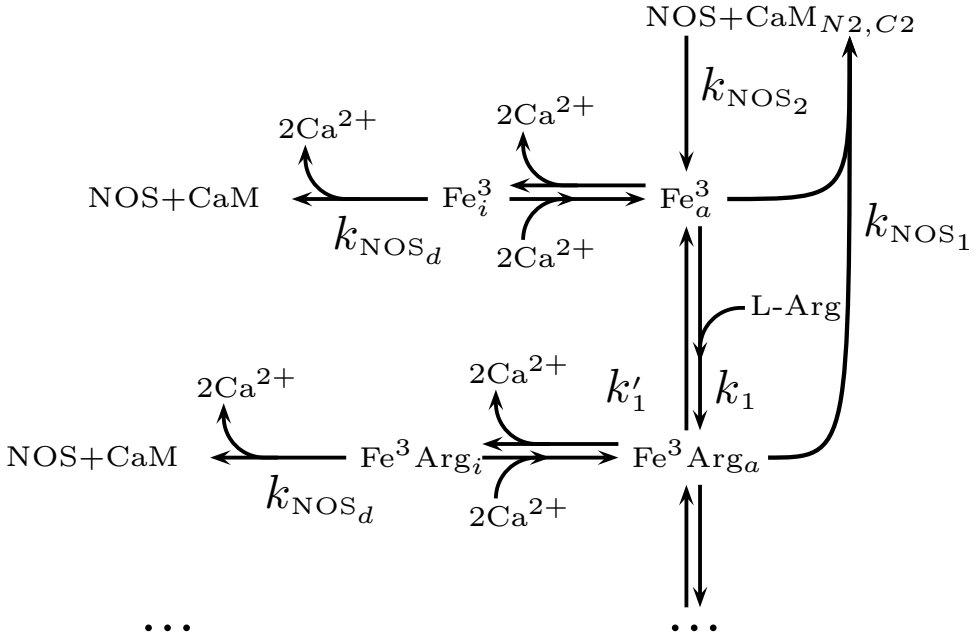

From Calcium to Nitric Oxide: first results

Equations resulting from our activation-reaction eNOS model were solved using the Matlab ODE suite(MATLAB 8.1, The MathWorks Inc., Natick, MA, 2013) with appropriate initial conditions. Concentration of eNOS, L-Arg, O_2 and CaM were set at physiological values reported in table 3.1. The system was balanced by slowly increasing Ca^{2+} concentration to reach a basal intracellular Ca^{2+} concentration of 50 nM. The system was considered at equilibrium when concentrations of every species in the model changes less than 1% on a timescale of 10^3 s.

Starting from this condition we have studied the reaction of the system to intracellular Ca^{2+} concentration changes both in case of rapid Ca^{2+} spikes or sustained Ca^{2+} increases. Ca^{2+} spikes was found to take place in a large variety of cells with a

duration of Ca^{2+} transient that can range from a few ms in excitable cells to around 1 s [12]. System reaction after a 1s Ca^{2+} spike is shown in figure 3.24.

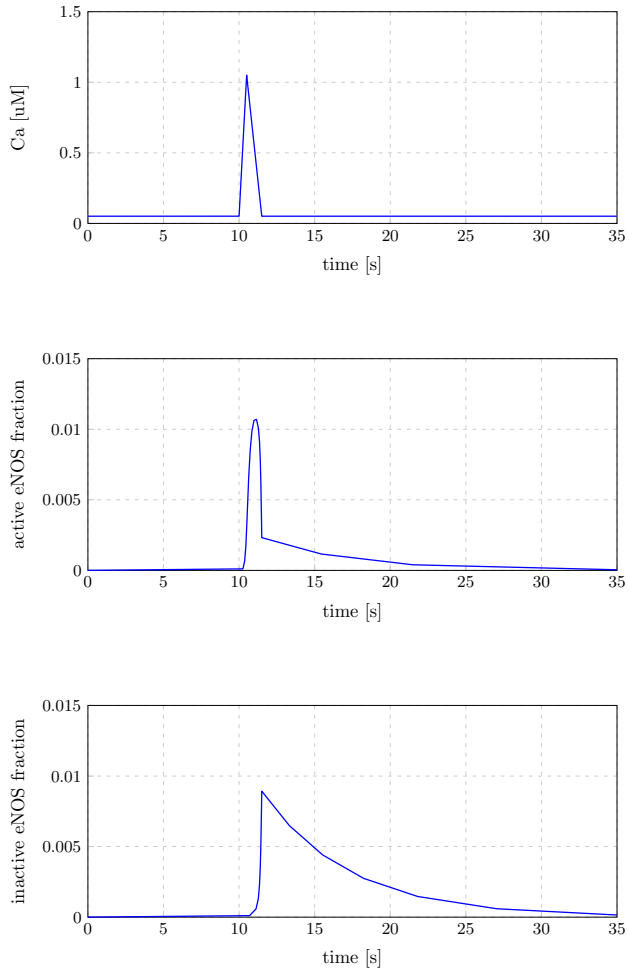

Figure 3.24: eNOS activation after a 1s full width at half amplitude (FWHA) Ca^{2+} spike. Total [eNOS] = 0.045 nM, [CaM] = 8.8 μM.

When intracellular Ca^{2+} increases, rapid enzyme activation takes place. Then Ca^{2+} rapidly comes back to basal value and activated enzyme is converted into the inactive form that dissociates from CaM in a few seconds. This mechanism provides a pool of inactive enzyme that lasts for a few seconds after Ca^{2+} decreases but can be rapidly restored to the active state whether if Ca^{2+} spike takes place.

eNOS activation in response to a sustained Ca^{2+} increase was also investigated. As we have just shown when saturated CaM become available, a burst in active enzyme concentration immediately starts. When Ca^{2+} concentration remains high the fraction of active enzyme continues to increase, reaching equilibrium after a few tens of seconds. Therefore we have considered active enzyme fraction at equilibrium and obtained its dependence on Ca^{2+} and CaM concentration. Simulations were carried

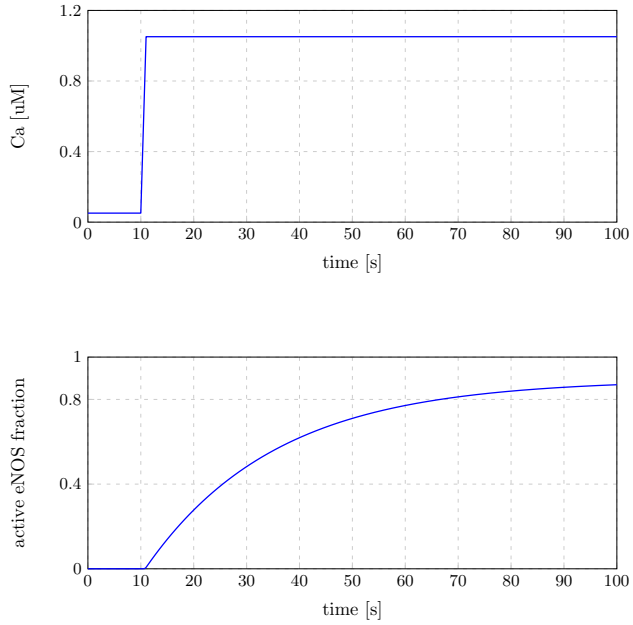

Figure 3.25: eNOS activation after sustained Ca^{2+} increase. Total[eNOS] = 0.045nM, [CaM] = 8.8μM.

out after equilibrating the system with different CaM concentration from 0 to 100 μM, then sustained Ca^{2+} signals with amplitude ranging between 0.1 to 3 μM were considered as model input. Resulting values for active and inactive enzyme fraction are reported in figures 3.26 and 3.27. Activation of the enzyme at different CaM concentration occurs when intracellular Ca^{2+} exceeds a threshold value of approximately 500 nM, such a prediction is not far from experimental values first reported by Cheung et al. who measured an activation value from 200 nM to 400 nM[25]. Moreover when CaM concentration falls under 2 μM this threshold rapidly increases. Recently Chen et al. performed measurements of eNOS activation under the condition of saturating Ca^{2+} level of 100 μM at different levels of CaM concentration. Their measurements shows that in such conditions eNOS EC_{50} for CaM is approximately of 60 nM[108]. Running our model in the same condition yielded a predicted EC_{50} of 24 nM that is a fairly good result considering measurement uncertainty and that our model is based on rate constant measured in rather different conditions.

We have observed that the dependence of the active enzyme fraction at equilibrium on CaM concentration shown a simple Michaeils Menten kinetics. A more complex behaviour was observed for the dependence on intracellular $[Ca^{2+}]_c$ due to its cooperative binding with CaM lobes. Thus we have developed a simple effective description of enzyme activation at steady state. We described eNOS binding to saturated CaM by means of simple Michaelis Menten kinetics:

$$\frac{[\mathrm{NOSCaM}]}{[\mathrm{NOS}]_0} = \frac{1}{1 + \frac{\alpha}{[\mathrm{CaM(Ca)}_{2N,2C}]}} \tag{3.21}$$

We modelled Ca^{2+} binding reaction with CaM considering independent cooperative binding at the two lobe, each one described by means of a Hills function.

$$\frac{[\mathrm{CaM(Ca)_{2N,2C}}]}{[\mathrm{CaM}]_0} = \left(\frac{[\mathrm{Ca^{2+}}]^n}{\beta + [\mathrm{Ca^{2+}}]^n}\right)^2 \tag{3.22}$$

On the whole eNOS active fraction versus Ca^{2+} and CaM concentration was interpolated by the relation:

$$\frac{[\mathrm{NOSCaM}]}{[\mathrm{NOS}]_0} = \frac{1}{1 + \frac{\alpha}{[\mathrm{CaM}]_0\left(\frac{[\mathrm{Ca^{2+}}]^n}{\beta + [\mathrm{Ca^{2+}}]^n}\right)^2}} \tag{3.23}$$

Such relation described quite well the simulated data, coefficients value obtained from Least-Square fit are $\alpha = 0.14\mu\mathrm{M}$ and $\beta = 2.49\mu\mathrm{M}^2$. The Hill coefficient n must be integer[40] and is interpreted as the number of ligand molecules that are required to bind to a receptor to produce a functional effect. For this reason we have set $n = 2$ according also with Hill coefficient for Ca^{2+} binding to CaM lobes reported in literature[71].

Ca^{2+} and CaM concentration do not affect only enzyme fraction that can reach the active state but also the speed of such process. We have investigated such effect introducing the activation time of the enzyme, defined at a fixed Ca^{2+} and CaM concentration as the time needed to reach half maximum of the active fraction achievable in such conditions. Results are shown in figure 3.28

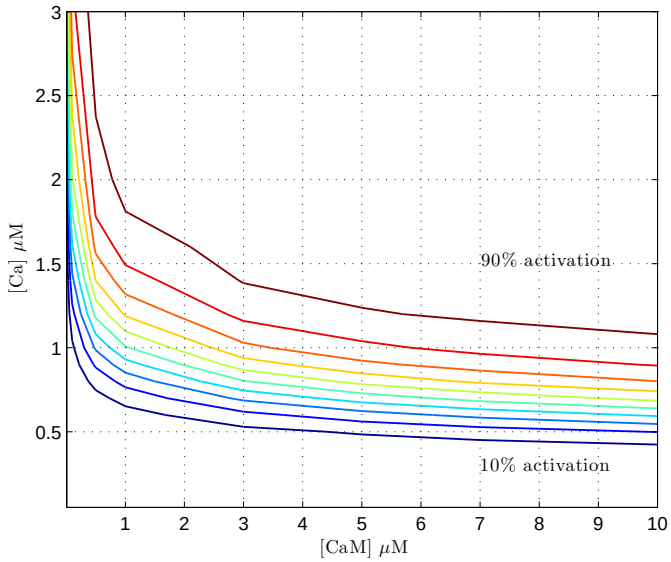

Figure 3.26: Contour plot of eNOS active fraction at equilibrium as a function of CaM concentration and sustained Ca^{2+} signals amplitude. eNOS activation starts at Ca^{2+} level above 0.5 μM. Simulations carried on at CaM concentration also higer than 10 μM did not show significative changes in activation pattern.

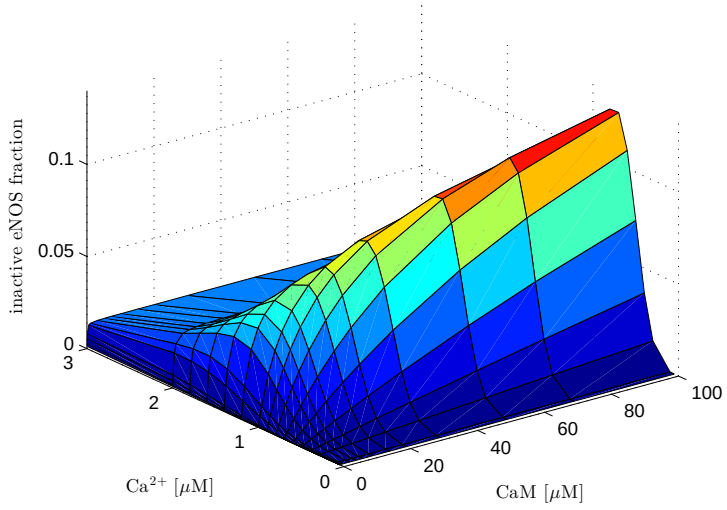

Figure 3.27: eNOS inactive fraction at equilibrium as a function of CaM and Ca^{2+} concentration.

.

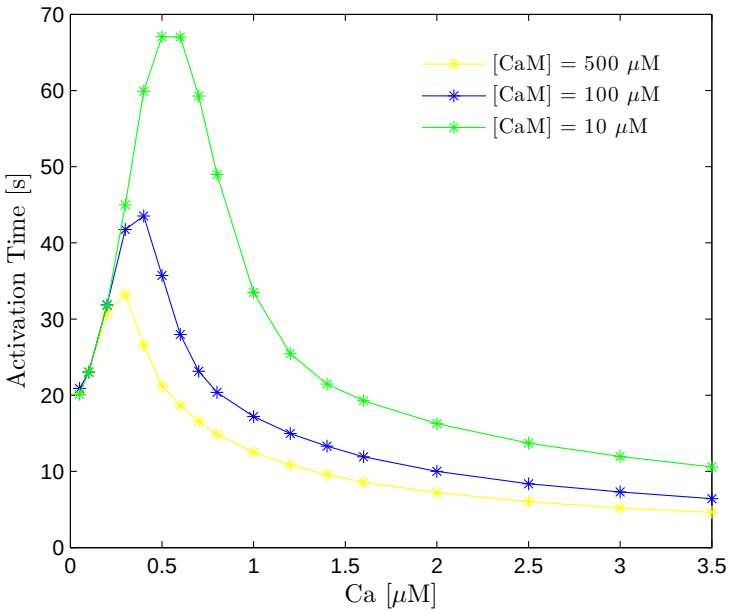

Figure 3.28: eNOS activation time as a function of Ca^{2+} and CaM concentration.

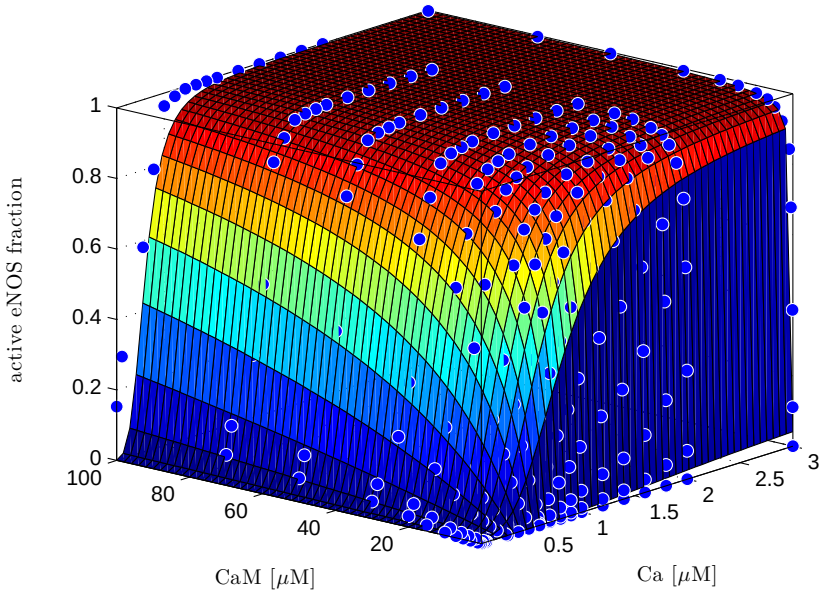

Figure 3.29: eNOS active fraction interpolated with equation 3.23.

3.2.3 NO production in focal PDT

The goal of this study was to use our model of eNOS activation to predict NO production rate in response to Ca^{2+} signals recorded in PDT experiments. Based on our studies, estimated $[Ca^{2+}]_c$ values of ~ 400 nM in PDT experiments seems insufficient to justify eNOS activation. Nevertheless, is well known that $[Ca^{2+}]_c$ represents only the mean Ca^{2+} concentration inside the cell and that specific cellular processes in different regions of the cell are regulated by localized regions of high Ca^{2+}, called microdomains[11]. Such domains are formed at sites where Ca^{2+} enters the cytoplasm either at the cell surface or at the internal stores and are a key element of Ca^{2+} signalling in which Ca^{2+} concentration can reach values up to 200-300 μM [63]. Moreover,it was also reported that eNOS co-localize with caveolin-1[2], a protein involved in formation and maintenance of small invaginations of plasma membranes called caveolae, that was demonstrated to be a site of Ca^{2+} microdomains[76], suggesting a fundamental role of microdomains also in eNOS activation.

Considering that fPDT triggers apoptosis in target and bystander cells, we could reasonably expect that local Ca^{2+} concentration is high enough to induce a maximum activation of eNOS. Thus, we have rescaled recorded Ca^{2+} signals by a factor of 10, in order to obtain an approximated estimate of Ca^{2+} concentration at the microdomain level, capable of inducing maximum eNOS activation.

Rescaled Ca^{2+} concentration values for every cell of a fPDT experiment, were used as input for eNOS activation model described in previous sections, whose equations were solved using the Matlab ODE suite (MATLAB 8.1, The MathWorks Inc., Natick, MA, 2013) in order to obtained NO production rate. Results are shown in figure 3.30. Since enzyme concentration inside the cell is unknown, NO production rate was normalized to enzyme concentration. Production rates for every cell obtained by this model were then inserted in the diffusion model defined by equations 3.13 and 3.14. NO concentration in bystander cells, selected at increasing distance from the target cell, was then compared to the enzymatic NO component of NO signal, extrapolated in section 3.2.1. Results shown in figure 3.31 suggest that this model of eNOS activation and NO production accounts for the rapid NO production evoked by PDT, under the hypotheses of Ca^{2+} microdomains involvement in enzyme activation, but fails to predict subsequent enzyme inactivation. These results also suggest that local Ca^{2+} dynamics is crucial to modulate NO production. Effectively, Ca^{2+} microdomains levels could be significantly higher than intracellular average concentration only during Ca^{2+} release from intracellular stores whereas, at a later stage, Ca^{2+} distribution inside the cytoplasm is homogenized by diffusion, providing one possible scheme to understand observed enzyme inactivation.

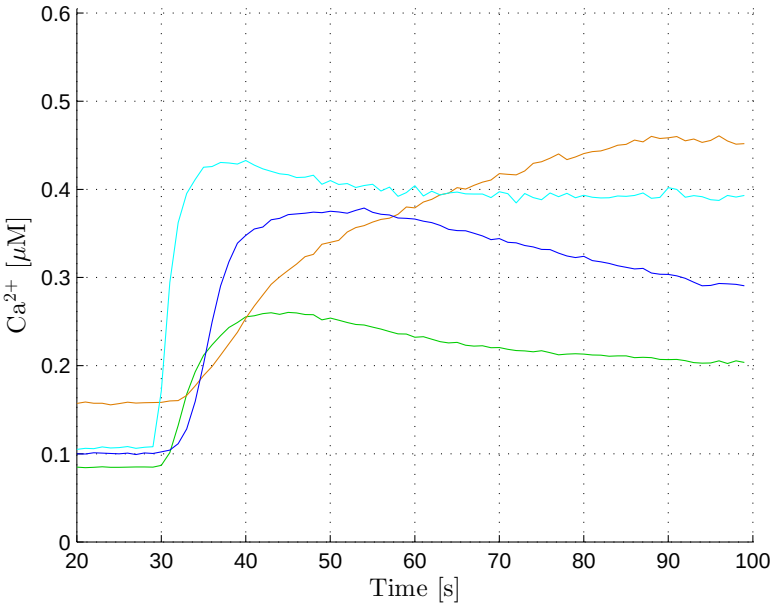

(a)

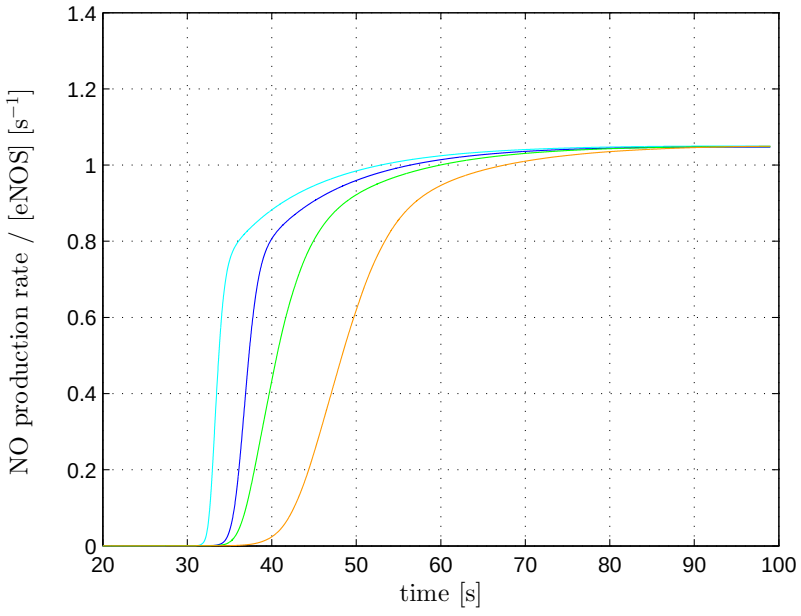

(b)

Figure 3.30: NO production rate expressed as a fraction of enzyme concentration (b), in response to recorded Ca^{2+} increase (a). Simulation parameters were set to [CaM] = 10 μM, [Arg] = 10 μM, [O_2] = 200 μM,$T = 37$°C, Ca^{2+} transient amplitude was scaled by a factor 10 in order to obtain an approximated estimate of Ca^{2+} concentration at the microdomain level.

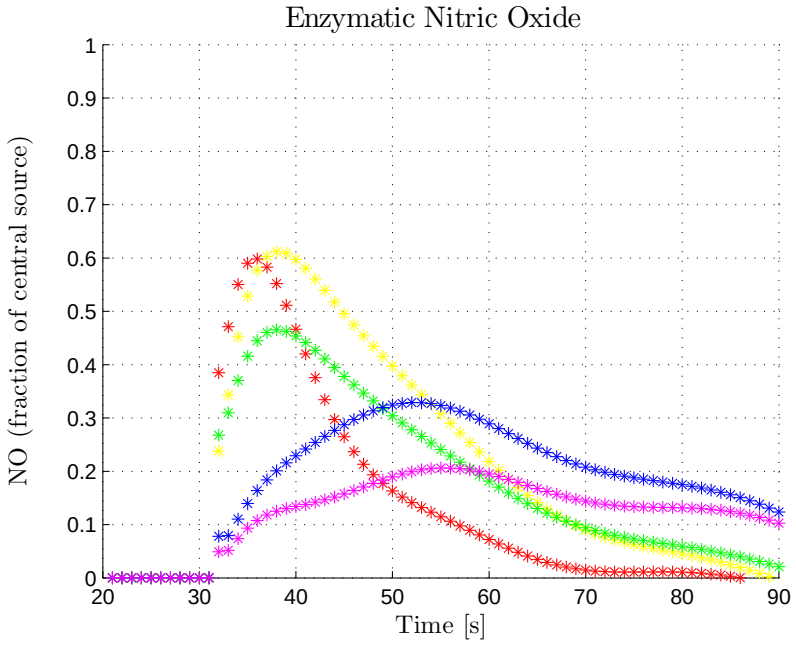

(a)

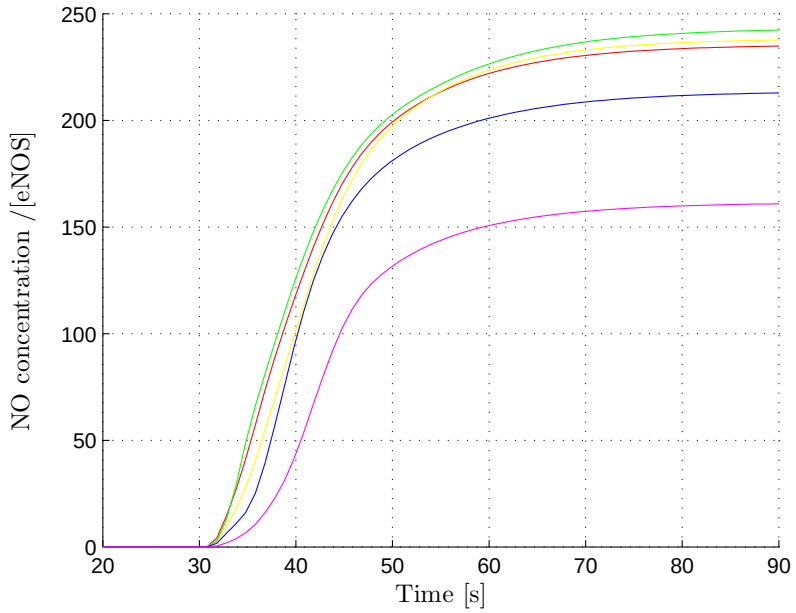

(b)

Figure 3.31: NO concentration within bystander cells selected at increasing distance from the photoactivation spot(b), NO concentration in the same cells due to NO production evoked by fPDT, extrapolated as described in section 3.2.1 (a).

Chapter 4

Conclusions and Future Perspectives

This study describes, for the first time, a new modality of NO production during fPDT. Similarly to radiotherapy, PDT is capable of triggering bystander responses in non-irradiated cells, acting as an inducer of immunogenic cell death, thus efficiently promoting antitumor immune response[100]. Prior work suggested the involvement of NO and RNS in bystander effects. However, the methods applied for NO tracking, such as chemiluminescence and spectroscopy, suffered from low spatial resolution and also required complicated instrumentation. The widely used fluorescent probes for NO, including o-diaminonaphthalene (DAN), o-diaminofluoresceins (DAFs) and o-diaminocyanines (DACs), react with oxidized NO products rather than NO itself, thus their fluorescence-response does not necessarily reflect real-time NO production[58].

The present work is based on the novel fluorescent probe CuFl, which reacts rapidly and specifically with NO over other potentially interfering molecules[59]. The method developed here for accurately analysing CuFl signals allowed us to dynamically monitor NO in real-time. Our data provide the first direct evidence of NO involvement in bystander response during PDT.

A newly developed method for voltage imaging of gap junction network showed that our cultured cells form a vast syncytium. Consistent with this result, pharmacological interference experiments with connexin inhibitors unveiled a crucial role played by gap junction channels in the bystander effect and cell-to-cell propagation of the apoptotic signal. Simultaneous imaging of CuFl and Fura-2 showed the NO signals in bystander cells spatially and temporally associated to an intercellular wave of Ca^{2+}.

The shape of NO signals indicates a dual mechanism whereby NO is directly released from the target cell upon photoactivation of AlPc and rapidly diffuses to bystander cells. NO levels are further elevated through enzymatic production driven by the Ca^{2+} wave which develops concurrently during PDT. By analyzing our data in the light of simple NO diffusion model, we were able to estimate the contribution of the diffusive component relative to enzymatic production, which amounts to at least 50% of the total NO signals evoked during PDT in bystander cells. Altogether, our data supported the notion that constitutive NOS activity is critical for the spreading of bystander responses and death signals following fPDT.

Therefore we developed a mathematical description of Ca^{2+}-mediated eNOS activation, based on experimental data reported in literature. The reliability of the model was tested by comparing significant parameters predicted by simulations with corresponding values found in literature. The model we propose is the first complete mathematical description of Ca^{2+} to NO transduction mediated by eNOS.

The discrepancy we find between experimental and simulation-based predictions of [NO] variation induced by $[Ca^{2+}]_c$ signals is easily ascribed to the role of Ca^{2+} microdomains in eNOS regulation. Reconstructing the dynamics of Ca^{2+} concentration in microdomains from $[Ca^{2+}]_c$ measurements is a complex task that can be achieved by stochastic deconvolution[15]. This will be subject of a future endeavour.

In summary, our data provide important new insight in the molecular mechanisms of PDT mediated bystander effect and support the notion that PDT represent a promising option for cancer treatment which is certainly worth further development. Understanding and quantitatively modelling the molecular basis of the effects evoked by this therapy, could in principle guide the use of appropriate combinations of Ca^{2+} modulating agents, NO-donors and gap junction enhancers to promote tumor eradication by maximizing bystander effects[83].

Appendices

Appendix A

eNOS model equations

A.1 NO production

$$\frac{d[\mathrm{Fe^{3+}}]}{dt} = -k_1[\mathrm{Arg}][\mathrm{Fe^{3+}}] + k_1'[\mathrm{Fe^{3+}Arg}] - k_2[\mathrm{Fe^{3+}}] + k_{14}[\mathrm{Fe^{3+}NO}] + k_{13}[\mathrm{Fe^{2+}NO}][\mathrm{O_2}] + k_8[\mathrm{Fe^{3+}NOHA}] - k_8'[\mathrm{Fe^{3+}}][\mathrm{NOHA}] \quad (A.1)$$

$$\frac{d[\mathrm{Arg}]}{dt} = 0 \quad (A.2)$$

$$\frac{d[\mathrm{Fe^{3+}Arg}]}{dt} = k_1[\mathrm{Fe^{3+}}][\mathrm{Arg}] - (k_3 + k_1')[\mathrm{Fe^{3+}Arg}] \quad (A.3)$$

$$\frac{d[\mathrm{Fe^{2+}}]}{dt} = k_2[\mathrm{Fe^{3+}}] - k_4[\mathrm{Fe^{2+}}][\mathrm{Arg}] + k_4'[\mathrm{Fe^{2+}Arg}] + k_9[\mathrm{Fe^{2+}NOHA}] - k_9'[\mathrm{Fe^{2+}}][\mathrm{NOHA}] \quad (A.4)$$

$$\frac{d[\mathrm{Fe^{2+}Arg}]}{dt} = k_3[\mathrm{Fe^{3+}Arg}] + k_4[\mathrm{Fe^{2+}}][\mathrm{Arg}] - k_4'[Fe^{2+}][\mathrm{Arg}] - k_5[\mathrm{Fe^{2+}Arg}][\mathrm{O_2}] + k_5'[\mathrm{Fe^{3+}O_2^-Arg}] \quad (A.5)$$

$$\frac{d[\mathrm{Fe^{3+}O_2^-Arg}]}{dt} = k_5[\mathrm{Fe^{2+}Arg}][\mathrm{O_2}] - k_6[\mathrm{Fe^{2+}O_2^-Arg}] - k_5'[\mathrm{Fe^{3+}O_2^-Arg}] \quad (A.6)$$

$$\frac{d[\mathrm{Fe^{2+}NOHA}]}{dt} = k_7[\mathrm{Fe^{3+}NOHA}] - k_{10}[\mathrm{Fe^{2+}NOHA}][\mathrm{O_2}] + k_{10}'[\mathrm{Fe^{3+}O_2^-NOHA}] - k_9[\mathrm{Fe2+NOHA}] + k_9'[\mathrm{Fe^{2+}}][NOHA] \quad (A.7)$$

$$\frac{d[\mathrm{Fe^{3+}O_2NOHA}]}{dt} = k_{10}[\mathrm{Fe^{2+}NOHA}][\mathrm{O_2}] - k_{11}[\mathrm{Fe^{3+}O^{2,-}NOHA}] - k_{10}'[\mathrm{Fe^{3+}O_2^-NOHA}] \quad (A.8)$$

$$\frac{d[\mathrm{Fe^{3+}NOHA}]}{dt} = k_6[\mathrm{Fe^{3+}O_2^-Arg}] - k_7[\mathrm{Fe^{3+}NOHA}] - k_8[\mathrm{Fe^{3+}NOHA}] + k_8'[\mathrm{Fe^{3+}}][\mathrm{NOHA}] \quad (A.9)$$

$$\frac{d[\mathrm{Fe^{3+}NO}]}{dt} = k_{11}[\mathrm{Fe^{3+}O_2^-NOHA}] - k_{14}[\mathrm{Fe^{3+}NO}] - k_{12}[\mathrm{Fe^{3+}NO}] \quad (A.10)$$

$$\frac{d[\mathrm{Fe^{2+}NO}]}{dt} = k_{12}[\mathrm{Fe^{3+}NO}] - k_{13}[\mathrm{Fe^{2+}NO}][\mathrm{O_2}] \quad (A.11)$$

$$\frac{d[\mathrm{NO}]}{dt} = k_{14}[\mathrm{Fe^{3+}NO}] \quad (A.12)$$

$$\frac{d[\mathrm{NOHA}]}{dt} = k_8[\mathrm{Fe^{3+}NOHA}] - k_8'[\mathrm{Fe^{3+}}][\mathrm{NOHA}] + k_9[\mathrm{Fe^{2+}NOHA}] - k_9'[\mathrm{Fe^{2+}}][\mathrm{NOHA}] \quad (A.13)$$

A.2 Enzyme activation

$$\frac{d[\mathrm{CaM}]}{dt} = -2(k_{N1}+k_{C1})[\mathrm{CaM}][\mathrm{Ca}^{2+}] + k'_{N1}[\mathrm{CaM_{1N}}] + k'_{C1}[\mathrm{CaM_{1C}}] + k_{NOSd}[\mathrm{NOSCaM}^*] \tag{A.14}$$

$$\frac{d[\mathrm{CaM_{1N}}]}{dt} = +2k_{N1}[\mathrm{CaM}][\mathrm{Ca}^{2+}] + k'_{C1}[\mathrm{CaM_{1N,1C}}] + 2k'_{N2}[\mathrm{CaM_{2N}}] - (k_{N2}+2k_{C1})[\mathrm{CaM_{1N}}][\mathrm{Ca}^{2+}] - k'_{N1}[\mathrm{CaM_{1N}}] \tag{A.15}$$

$$\frac{d[\mathrm{CaM_{1C}}]}{dt} = +2k_{C1}\mathrm{CaM}[\mathrm{Ca}^{2+}] + k'_{N1}[\mathrm{CaM_{1N,1C}}] + 2k'_{C2}[\mathrm{CaM_{2C}}] - (k_{C2}+2k_{N1})[\mathrm{CaM_{1C}}][\mathrm{Ca}^{2+}] - k'_{C1}[\mathrm{CaM_{1C}}] \tag{A.16}$$

$$\frac{d[\mathrm{CaM_{2N}}]}{dt} = +k_{N2}[\mathrm{CaM_{1N}}][\mathrm{Ca}^{2+}] + k'_{C1}[\mathrm{CaM_{2N,1C}}] - 2k'_{N2}[\mathrm{CaM_{2N}}] - 2k_{C1}[\mathrm{CaM_{2N}}][\mathrm{Ca}^{2+}] \tag{A.17}$$

$$\frac{d[\mathrm{CaM_{2C}}]}{dt} = +k_{C2}[\mathrm{CaM_{1C}}][\mathrm{Ca}^{2+}] + k'_{N1}[\mathrm{CaM_{1N,2C}}] - 2k_{N1}[\mathrm{CaM_{2C}}][\mathrm{Ca}^{2+}] - 2k'_{C2}[\mathrm{CaM_{2C}}] \tag{A.18}$$

$$\frac{d[\mathrm{CaM_{1N,1C}}]}{dt} = +2k_{C1}[\mathrm{CaM_{1N}}][\mathrm{Ca}^{2+}] + 2k_{N1}[\mathrm{CaM_{1C}}][\mathrm{Ca}^{2+}] + 2k'_{N2}[\mathrm{CaM_{2N,1C}}] + 2k'_{C2}[\mathrm{CaM_{1N,2C}}] - (k'_{N1}+k'_{C1}-k_{N2}[\mathrm{Ca}^{2+}]-k_{C2}[\mathrm{Ca}^{2+}])[\mathrm{CaM_{1N,1C}}] \tag{A.19}$$

$$\frac{d[\mathrm{CaM_{1N,2C}}]}{dt} = +2k_{N1}[\mathrm{CaM_{2C}}][\mathrm{Ca}^{2+}] + k_{C2}[\mathrm{CaM_{1N,1C}}][\mathrm{Ca}^{2+}] + 2k'_{N2}[\mathrm{CaM_{2N,2C}}] - k'_{N1}[\mathrm{CaM_{1N,2C}}] - 2k'_{C2}[\mathrm{CaM_{1N,2C}}] - k_{N2}[\mathrm{CaM_{1N,2C}}][\mathrm{Ca}^{2+}] \tag{A.20}$$

$$\frac{d[\mathrm{CaM_{2N,1C}}]}{dt} = +2k_{C1}[\mathrm{CaM_{2N}}][\mathrm{Ca}^{2+}] + k_{N2}[\mathrm{CaM_{1N,1C}}][\mathrm{Ca}^{2+}] + 2k'_{C2}[\mathrm{CaM_{2N,2C}}] - k'_{C1}[\mathrm{CaM_{2N,1C}}] - 2k'_{N2}[\mathrm{CaM_{2N,1C}}] - k_{C2}[\mathrm{CaM_{2N,1C}}][\mathrm{Ca}^{2+}] \tag{A.21}$$

$$\frac{d[\mathrm{CaM_{2N,2C}}]}{dt} = +k_{C2}[\mathrm{CaM_{2N,1C}}][\mathrm{Ca}^{2+}] + k_{N2}[\mathrm{CaM_{1N,2C}}][\mathrm{Ca}^{2+}] - 2(k'_{C2} + k'_{N2})[\mathrm{CaM_{2N,2C}}] - k_{NOS1}[\mathrm{CaM_{2N,2C}}][\mathrm{NOS}] + k_{NOS2}[\mathrm{NOSCaM}] \tag{A.22}$$

$$\frac{d[\mathrm{NOS}]}{dt} = -k_{NOS1}[\mathrm{CaM_{2N,2C}}][\mathrm{NOS}] + k_{NOS2}[\mathrm{NOSCaM}] + k_{NOSd}[\mathrm{NOSCaM}^*] \tag{A.23}$$

$$\frac{d[\mathrm{NOSCaM}]}{dt} = -k_{NOSd}[\mathrm{NOSCaM}^*] - k_{NOS2}[\mathrm{NOSCaM}] + k_{NOS1}[\mathrm{CaM_{2N,2C}}][\mathrm{NOS}] \tag{A.24}$$

$$[\mathrm{NOSCaM}^*] = \frac{[\mathrm{NOSCaM}]}{[\mathrm{Ca}^{2+}] * k_{\mathrm{NOS}_{eq}}} \tag{A.25}$$

Appendix B

Fluorescence imaging with dual wavelength indicators

Optical measurements of the intracellular concentration of selected ion species is a well known technique to access ions concentration, such as Ca^{2+}, with high spatial and temporal resolutions. Such techniques rely on the ability of the fluorescent probe, namely fluorescent dye, to provide useful information about its environment by suitable changes in its fluorescent properties in response to changes in the parameter to be measured. For biological applications changes in fluorescent yield, shift in the excitation or emission spectra or a combination of these effects are considered appropriate.

In dual wavelength indicators a shift in excitation (or emission) spectra takes place when target ions bind to the fluorophore, therefore excitation spectra of free and bound fluorophore cross in a point called isosbestic point. Such properties allow to get ratio-metric measurements of target ions concentration by evaluating the ratio between fluorescence emission at two wavelengths located on opposite sides relative to the isosbestic point. Considering ratio measurements rather than single wavelength fluorescence increase leads to a great improvement in target ion concentration assessment and neutralizes artefacts caused by photo-bleaching. Imaging with dual excitation fluorophores requires the sequential excitation at two wavelengths that can be achieved by switching rapidly between two light sources.

In order to achieve quantitative imaging of Ca^{2+} ions concentration we need to link it with the fluorescence ratio. Fluorescence emission by two wavelengths dyes is characterized by four parameters S_{f_1} and S_{f_2} for Ca^{2+}-free dye at wavelength λ_1 and λ_2 and S_{b_1} and S_{b_2} for Ca^{2+}-bound dye. Then fluorescence ratio results:

$$F_1 = S_{f_1}[\mathrm{P}] + S_{b_1}[\mathrm{CaP}] \tag{B.1}$$

$$F_2 = S_{f_2}[\mathrm{P}] + S_{b_2}[\mathrm{CaP}] \tag{B.2}$$

$$R = \frac{F_1}{F_2} = \frac{S_{f_1} + S_{b_1}\frac{[\mathrm{Ca}^{2+}]}{k_{d,p}}}{S_{f_2} + S_{b_2}\frac{[\mathrm{Ca}^{2+}]}{k_{d,p}}} \tag{B.3}$$

where $k_{d,p}$ is the dissociation constant, [P] is the concentration of free fluorophore, [CaP] the concentration of bound fluorophore and the equilibrium condition [CaP] =

$[P][Ca^{2+}]/k_{d,p}$ has been used. Rearranging such relation, introducing $R_{min} = S_{f_1}/S_{f_2}$, that means the ratio when Ca^{2+} concentration approaches zero, and $R_{max} = S_{b_1}/S_{b_2}$, the ratio at saturating Ca^{2+} concentration, we obtained the Grynkiewicz equation:

$$[Ca^{2+}]_c = \frac{k_{d,p}(R - R_{min})}{R_{max} - R} \left(\frac{F_f}{F_b}\right) \tag{B.4}$$

Notice that the applicability of the Grynkewicz equation depends on the assumption of a 1:1 dye-Ca^{2+} complexation with a sufficiently diluted medium where fluorescence is proportional to concentration. Moreover R_{min}, R_{max} and F_f/F_b must be measured on the same instrumentations to calibrate the system.

Fura-2 (Invitrogen/Molecular Probes) is an extensively used ratiometric Ca^{2+} dye. For imaging experiments, cells were loaded with Fura-2 acetoxymethyl (AM) esters, an analogue of Fura-2 that can passively diffuse across cell membranes. Once inside the cells, these esters are cleaved by intracellular esterases to yield cell-impermeant fluorescent indicator[99].

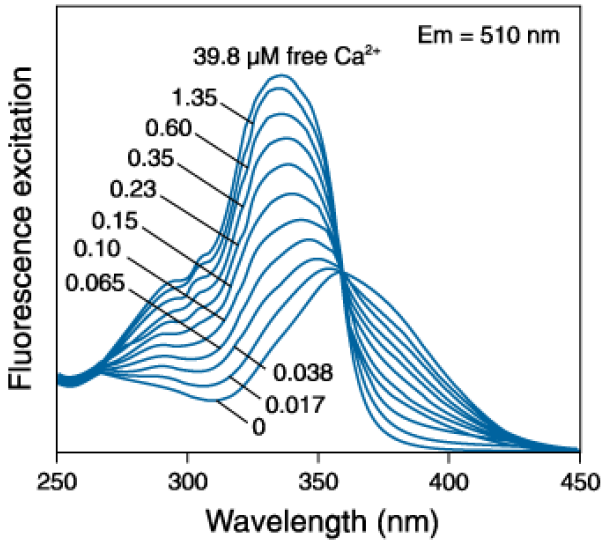

Figure B.1: Fura-2 ratiometric dye for calcium imaging excitation spectra

Appendix C

Tests and calibration

C.1 Fura-2 Calibration

As previously introduced in appendix B, measurements of intracellular Ca^{2+} concentration were made from ratio values by application of the Grynkiewicz equation:

$$[Ca^{2+}]_c = \frac{k_{d,p}(R - R_{min})}{R_{max} - R} \left(\frac{F_f}{F_b}\right) \tag{C.1}$$

where R is the ratio between fluorescence emission intensity excited at 365 nm divided by the intensity excited at 385 nm. Both fluorescence emissions are a sum of different contribution that form the background of recorded signals and must be subtracted in order to obtain a reliable estimate of intracellular Ca^{2+}. Particularly, fluorescence emission at 365nm and 385 nm excitation wavelength are an overlap of Fura-2 emission, cells autofluorescence, AlPc fluorescence emission and crossover emission of CuFl (Bleed Through) due to its broad spectral profile. Cell autofluorescence and AlPc fluorescence were measured from cells loaded with the PS only, subjected to the same experimental protocol used in PDT experiments, comprehensive of single cell photoactivation. CuFl bleed-through was measured from cell cultures loaded with the PS and CuFl and was reported as the ratio between the emission at 365nm or 385nm and that at 460nm excitation wavelengths. R_{min} and R_{max} refer to minimum and maximum ratio values recorded in situ with 10μM ionomycin in the presence of 2mM EGTA solution and 20mM Ca^{2+} solution, respectively; $\frac{F_f}{F_b}$ is the ratio of the fluorescence values of the Ca^{2+}-free and Ca^{2+} bound forms at 380 nm; the k_d of Fura2 at 22°C was assumed to be 280nM[46]. Every calibration measurement was repeated with at least three different samples, mean values of every parameter were reported in table C.1 on the following page.

Table C.1: Mean values for calibration parameters.

Camera offset	1488
$F_{AlPc,365} + F_{Auto,365}$	37
$F_{AlPc,385} + F_{Auto,385}$	48
$F_{AlPc,460} + F_{Auto,460}$	75
$\frac{F_{CuFl,365}}{F_{CuFl,460}}$	1.64%
$\frac{F_{CuFl,365}}{F_{CuFl,460}}$	5.88%
s	11.06
R_{min}	0.42
R_{max}	13.04

C.2 AlPc effects on dyes fluorescent emission

In order to avoid possible direct effects of AlPc or its photo-activation by-products on Fura-2 or CuFl fluorescence emissions experimental test were carried on.

CuFl test experiments were carried on in small ($\sim 100\mu$m diameter) aqueous vesicles of the solution formed in Sylgard on a coverslip. The same aqueous solution used for cell perfusion during imaging experiments, addicted with 20μM CuFl and 10μM AlPc, was disperded as small vesicles by stirring 10μl into 100μl Sylgard, dropping on a coverslip and allowing 30min for air bubble to come out[19]. Sample position was adjusted in order to observe a single vesicle in the frame and its fluorescence emission was monitored during 60s irradiation with 671nm solid state laser focused on the specimen as previously described. Resulting fluoresce emission was not affected by AlPc photo-activation and resulting singlet oxygen production.

Comparable experiments were carried for Fura-2 with similar solution addicted with 10μM AlPc and Fura-2 15 μM. Due the opacity of Sylgard to UV radiation such experiments were conducted on a drop of solution placed above a coverslip. Only a small increase in Fura-2 emission both at 360nm and 380nm excitation wavelengths were registered. Such increase also results in an enhancement of fluorescence ratio. This result does not affect Ca^{2+} measurements carried on in PDT experiments because indeed in that case activated AlPc is only present in target cell and not in nearby bystander cells.

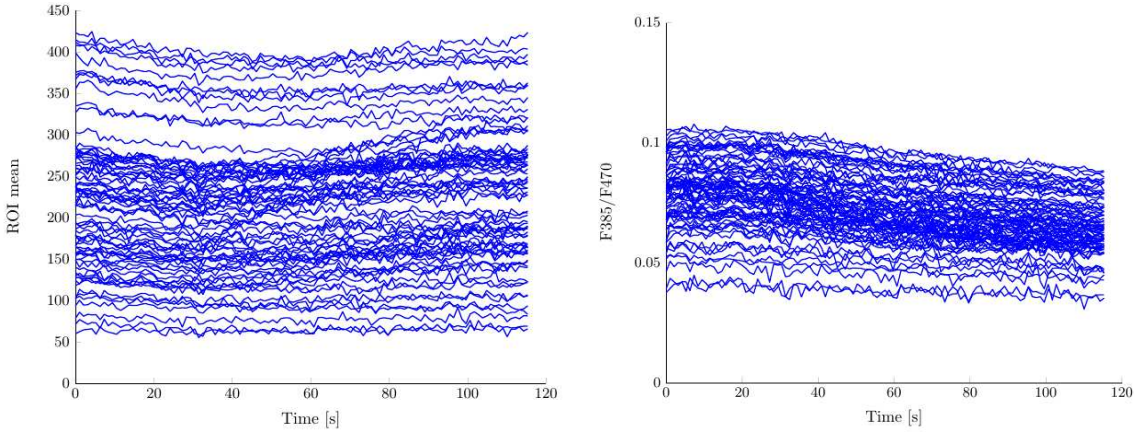

Figure C.1: CuFl bleed through at 385nm excitation wavelength during AlPc photoactivation, showed as raw fluorescence data and fraction of fluorescence at 460nm excitation.

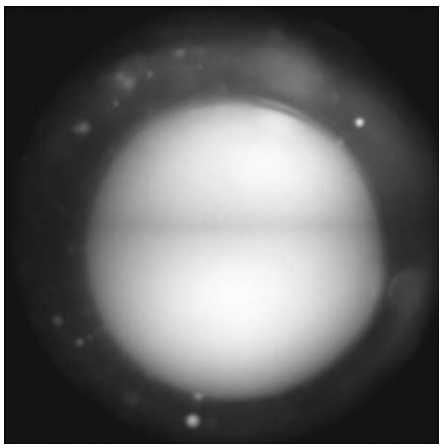

Figure C.2: CuFl aqueous vesicle in Sylgard

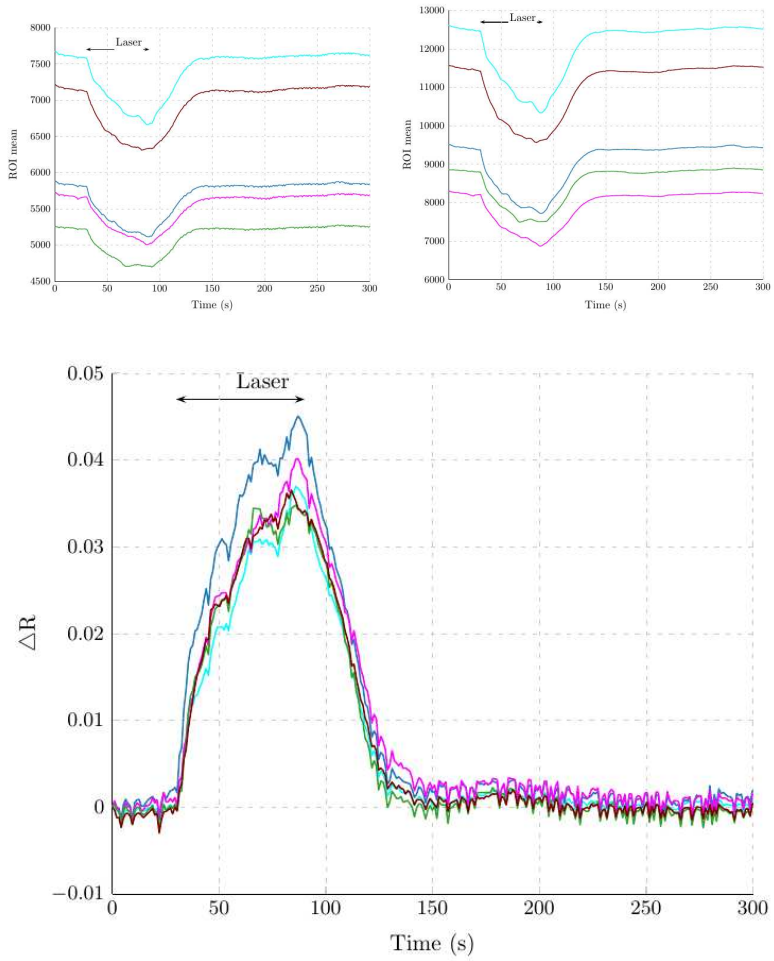

Figure C.3: Fura2 fluorescence emission and ratio in a drop of experimental solution during AlPc photoactivation

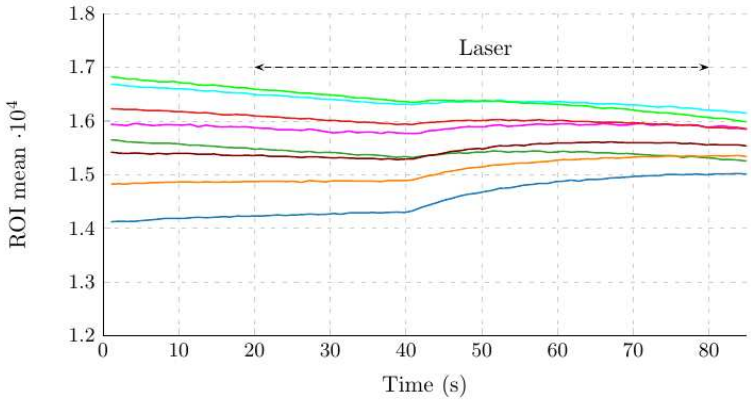

Figure C.4: CuFl fluorescence emission into an aqueous vesicle in Sylgard during AlPc photoactivation

Bibliography

[1] H. M. Abu-Soud et al. “Electron transfer,oxygen binding, and nitric oxide feedback inhibition in endothelial nitric-oxide synthase.” In: *J. Biol. Chem.* 275 (2000), 17349–17357.

[2] El-Yazbi AF et al. “Smooth muscle NOS, colocalized with caveolin-1, modulates contraction in mouse small intestine.” In: *J Cell Mol Med.* 12.4 (2008), 1404–1415.

[3] Patrizia Agostinis et al. “Photodynamic Therapy of Cancer: An Update”. In: *Ca. Cancer J. Clin.* 61 (2011), pp. 250–281.

[4] Wendy K. Alderton, Chris E. Cooper, and Richard G. Knowels. “Nitric oxide synthases : structure, function and inhibition”. In: *Biochem. J.* 357 (2001), pp. 593–615.

[5] M.R. Andersen, L.R. Walker, and S. Stender. “Reduced endothelial nitric oxide synthase activity and concentration in fetal umbilical veins from maternal cigarette smoker”. In: *Am. J. Obstet. Gynecol.* 191 (2004), pp. 346–351.

[6] F. Anselmi et al. “ATP release through connexin hemichannels and gap junction transfer of second messengers propagate Ca2+ signals across the inner ear”. In: *PNAS* 105.48 (2008), pp. 18770–5.

[7] Mika Aoyagi et al. “Structural basis for endothelial nitric oxide synthase binding to calmodulin”. In: *The EMBO Journal* 22.4 (2003), pp. 766–775.

[8] Michael T. Barbe, Hannah Monyer, and Roberto Bruzzone. “Cell-Cell Communication Beyond Connexins: The Pannexin Channels”. In: *Physiology* 21 (2006), pp. 103–114.

[9] Rajamanickam Baskar. “Emerging role of radiation induced bystander effects: Cell communications and carcinogenesis”. In: *Genome Integrity* 1.13 (2010).

[10] V. Berka, P. F. Chen, and A. L. Tsai. “Spatial relationship between L-arginine and heme binding sites of endothelial nitric-oxide synthase”. In: *J. Biol. Chem.* 271 (1996), 33293–33300.

[11] Michael J. Berridge. “Calcium microdomains: Organization and function”. In: *Cell Calcium* 40 (2006), 405–412.

[12] Michael J. Berridge. “Unlocking the secrets of cell signaling”. In: *Annu. Rev. Physiol.* 67 (2005), 1–21.

[13] Michael J. Berridge and P. Lipp. “The versatility and universality of calcium signalling.” In: *Nat Rev Mol Cell Biol* 1.1 (2000), 11–21.

[14] D.J. Black, Quang-Kim Tran, and Anthony Persechini. “Monitoring the total available calmodulin concentration in intact cells over the physiological range in free Ca2+”. In: *Cell Calcium* 35 (2004), pp. 415–425.

[15] Mario Bortolozzi, Andrea Lelli, and Fabio Mammano. “Calcium microdomains at presynaptic active zones of vertebrate hair cells unmasked by stochastic deconvolution.” In: *Cell Calcium* 44 (2008), 158—168.

[16] V. Bronte et al. “IL-4-induced arginase 1 suppresses alloreactive T cells in tumor-bearing mice.” In: *J. Immunol.* 170.1 (2003), pp. 270–278.

[17] Guy C. Brown. “Regulation of mitochondrial respiration by nitric oxide inhibition of cytochrome c oxidase”. In: *Biochimica et Biophysica Acta* 1504 (2001), pp. 46–57.

[18] Susan E. Brown, Stephen R. Martin, and Peter. “Kinetic Control of the Dissociation Pathway of Calmodulin-Peptide Complexes”. In: *J. Biol. Chem.* 272 (1997), pp. 3389–3397.

[19] M. Canepari et al. “Photochemical and pharmacological evaluation of 7-nitroindolynyl- and 4-methoxy-7-nitroindolinyl-amino acids as novel, fast caged neurotransmitters”. In: *Journal of Neuroscience Methods* 112 (2001), pp. 29–42.

[20] Ana P. Castano, Pawel Mroz, and Michael R. Hamblin. “Photodynamic therapy and anti-tumour immunity”. In: *Nature Reviews Cancer* 6 (2006), pp. 535–545.

[21] Wei C.C et al. “Structure of tetrahydrobiopterin tunes its electron transfer to the heme-dioxy intermediate in nitric oxide synthase”. In: *Biochemistry* 42.7 (2003), 1969–1977.

[22] Wei C.C et al. “The three nitric-oxide synthases differ in their kinetics of tetrahydrobiopterin radical formation, heme-dioxy reduction, and arginine hydroxylatione”. In: *J. Biol. Chem.* 280 (2005), 8929–8935.

[23] Kejing Chen and Aleksander S. Popel. “Theoretical analysis of biochemical pathways of nitric oxide release from vascular endothelial cells”. In: *Free Radical Biology & Medicine* 41 (2006), pp. 668–680.

[24] Yih-Fung Chen et al. “Remodeling of calcium signaling in tumor progression”. In: *J Biomed Sci* 20 (2013), p. 23.

[25] W. Y. Cheung. “Calmodulin plays a pivotal role in cellular regulation”. In: *Science* 207.4426 (1980), 19–27.

[26] E. I. Closs et al. “Substrate supply for nitric-oxide synthase in macrophages and endothelial cells: role of cationic amino acid transporters.” In: *Mol. Pharmacol.* 57 (2000), pp. 68–74.

[27] Brian R. Crane et al. “Structure of Nitric Oxide Synthase Oxygenase Dimer with Pterin and Substrate”. In: *Science* 279 (1998), pp. 2121–2126.

[28] S. Dimmeler and J. Haendeler. “Suppression of apoptosis by nitric oxide via inhibition of interleukin-1beta-converting enzyme (ICE)-like and cysteine protease protein (CPP)-32-like proteases.” In: *J Exp Med* 185.4 (1997), pp. 601–607.

[29] Williams DLH. *Nitrosation reactions and the chemistry of nitric oxide*. 1th. Elsevier, 2004.

[30] Kim Y. E., J. Chen, and et al. “Monitoring apoptosis and neuronal degeneration by real-time detection of phosphatidylserine externalization using a polarity sensitive indicator of viability and apoptosis”. In: *Nat Protoc* 5.8 (2010), pp. 1396–1405.

[31] Guido C. Faas et al. “Calmodulin as a Direct Detector of Ca2+ Signals”. In: *Nat Neurosci.* 14.3 (2011), pp. 301–304.

[32] E. Fassen and A. F. Vanin. *Radicals for life*. 1th. Elsevier, 2007, pp. 3–16.

[33] Dahl G. and Keane RW. “Pannexin: from discovery to bedside in 11±4 years?” In: *Brain Res.* 3 (2012), pp. 150–9.

[34] E.P. Garvey et al. “Purification and Characterization of the Constitutive Nitric-Oxide Synthase from Human Placenta”. In: *Archives of Biochemistry and Biophysics* 311.2 (1994), pp. 235–241.

[35] E. Gomes, R., R. D. Almeida, et al. “Nitric oxide modulates tumor cell death induced by photodynamic therapy through a cGMP-dependent mechanism.” In: *Photochem Photobiol* 76.4 (2002), pp. 423–430.

[36] A. C. Gorren and B. . Mayer. “Tetrahydrobiopterin in nitric oxide synthesis: a novel biological role for pteridines”. In: *Curr. Drug Metab.* 3 (2002), 133–157.

[37] Grzegorz Grynkiewicz, Martin Poenie, and Roger Y. Tsien. “A New Generation of Ca2+ Indicators with Greatly Improved Fluorescence Properties”. In: *J. Biol. Chem.* 260.6 (1985), pp. 3440–3450.

[38] Catherine N. Hall and John Garthwaite. “What is the real physiological NO concentration in vivo?” In: *Nitric Oxide* 21 (2009), pp. 92–103.

[39] Victor H Hernandez et al. “Unitary permeability of gap junction channels to second messengers measured by FRET microscopy”. In: *Nature Methods* 4 (2007), pp. 353–358.

[40] A. V. Hill. “The possible effects of the aggregation of the molecules of hemoglobin on its dissociation curves.” In: *Proceedings of physiological society* 1 (1910), pp. 4–7.

[41] Louis J. Ignarro et al. “Endothelium-derived relaxing factor produced and released from artery and vein is nitric oxide”. In: *PNAS* 84 (1987), pp. 9265–9269.

[42] Lee JM et al. “Ion channels and transporters in cancer. 4. Remodeling of Ca(2+) signaling in tumorigenesis: role of Ca(2+) transport.” In: *Am J Physiol Cell Physiol* 301.5 (2011), pp. 969–976.

[43] Michael A. Marletta John W. Denninger. "Guanylate cyclase and the cNO/cGMP signaling pathway". In: *Biochimica et Biophysica Acta* 1411 (1999), pp. 334–350.

[44] Eric Jones, Travis Oliphant, Pearu Peterson, et al. *SciPy: Open source scientific tools for Python*. [Online; accessed 2014-06-26]. 2001–. URL: `http://www.scipy.org/`.

[45] Groves JT and Wang CC. "Nitric oxide synthase: models and mechanisms". In: *Curr. Opin. Chem. Biol.* 4.6 (2000), pp. 687–695.

[46] J.P.Y. Kao. "Measuring [Ca2+] with fluorescent indicators". In: *Methods Cell Biol* 40 (1994), pp. 155–181.

[47] Ahnert Karsten and Abel Markus. "Numerical differentiation of experimental data: local versus global methods". In: *Computer Physics Communications* 177 (2007), pp. 764–774.

[48] James Keener and James Sneyd. *Mathematical Physiology*. 1th. Springer, 1998.

[49] E. L. King and J. Altman C. "Ethinylestradiol does not enhance the expression of nitric oxide synthase in bovine endothelial cells but increases the release of bioactive nitric oxide by inhibiting superoxide anion production." In: *J. Phys. Chem.* 60 (1956), pp. 1375–1378.

[50] Richard G. Knowles and Salvador Moncada. "Nitric oxide synthases in mammals". In: *Biochem. J.* 298 (1994), pp. 249–258.

[51] W.H. Koppenol and J.G. Traynham. "Say NO to nitric oxide: Nomenclature for nitrogen- and oxygen-containing compounds". In: *Methods in Enzymology*. Vol. 268. Elsevier, 1996, pp. 3–7.

[52] Hitoshi Kuboniwa et al. "Solution structure of calcium-free calmodulin". In: *Nature Structural Biology* 2 (1995), pp. 768–776.

[53] Leon L., J.F Jeannin, and et al. "Post-translational modification induced by nitric oxide (NO): implication in cancer cells apoptosis". In: *Nitric Oxide* 19.2 (2008), pp. 77–83.

[54] Zweier Jay L., Alexandre Samouilov, and Periannan Kuppusamy. "Non-enzymatic nitric oxide synthesis in biological systems". In: *Biochimica et Biophysica Acta* 1411 (1999), pp. 250–262.

[55] Zweier Jay L. et al. "Enzyme-independent formation of nitric oxide in biological tissues". In: *Nat. Med.* 1 (1995), pp. 804–809.

[56] Jr. Lancaster J. R. "A tutorial on the diffusibility and reactivity of free nitric oxide." In: *Nitric Oxide* 1.1 (1997), pp. 18–30.

[57] L. Leon and J. F. Jeannin. "Post-translational modifications induced by nitric oxide(NO): implication in cancer cells apoptosis." In: *Nitric Oxide* 19.2 (2008), pp. 77–83.

[58] Mi Hee Lim, Dong Xu, and Stephen J. Lippard. "Visualization of nitric oxide in living cells by a copper-based fluorescent probe". In: *Nature Chemical Biology* 2 (2006), pp. 375–380.

[59] Mi Hee Lim et al. “Direct Nitric Oxide Detection in Aqueous Solution by Copper(II) Fluorescein Complexes”. In: *J. Am. Chem. Soc.* 128 (2006), pp. 14364–14373.

[60] Jianwei Liu, Guillermo Garcia-Cardena, and William C. Sessa. “Palmitoylation of endothelial nitric oxide synthase is necessary for optimal stimulated release of nitric oxide: implications for caveolae localization”. In: *Biochemistry* 35 (1996), pp. 13277–13281.

[61] Xiaoping Liu et al. “Accelerated reaction of nitric oxide with O2 within the hydrophobic interior of biological membranes”. In: *PNAS* 95.5 (1998), pp. 355–360.

[62] Xiaoping Liu et al. “Nitric Oxide Diffusion Rate is Reduced in the Aortic Wall”. In: *Biophysical Journal* 94 (2008), pp. 1880–1889.

[63] R. Llinas, M Sugimori, and RB Silver. “Microdomains of high calcium concentration in a presynaptic terminal”. In: *Science* 256.5057 (1992), pp. 677–679.

[64] V. Lubrano et al. “The effect of lipoproteins on endothelial nitric oxide synthase is modulated by lipoperoxides”. In: *Eur. J. Clin. Invest* 33 (2003), pp. 117–125.

[65] T. Malinski et al. “Diffusion of Nitric Oxide in the Aorta Wall Monitored in Situ by Porphyrinic Microsensors”. In: *Biochem. Biophys. Res. Commun.* 193 (1993), pp. 1076–1082.

[66] S. Marchal et al. “Evidence of two distinct oxygen complexes of reduced endothelial nitric oxide synthase”. In: *J. Biol. Chem.* 279 (2004), 19824–19831.

[67] Michael A. Marletta. “Nitric Oxide Signaling”. In: *Encyclopedia of Biological Chemistry*. Ed. by William J. Lennarz and M. Daniel Lane. Vol. 3. Elsevier, 2004, pp. 62–65.

[68] Jonathan L. McMurry et al. “Rate, affinity and calcium dependence of nitric oxide synthase isoform binding to the primary physiological regulator calmodulin”. In: *FEBS Journal* 278 (2011), 4943–4954.

[69] Lindsey E. McQuade and Stephen J. Lippard. “Fluorescence-Based Nitric Oxide Sensing by Cu(II) Complexes That Can Be Trapped in Living Cells”. In: *Inorganic Chemistry* 49.16 (2010), pp. 7464–7471.

[70] C. J. Meininger et al. “Impaired nitric oxide production in coronary endothelial cells of the spontaneously diabetic BB rat is due to tetrahydrobiopterin deficiency”. In: *Biochem. J.* 349 (2000), pp. 353–356.

[71] J. S. Mills and J. D. Johnson. “Metal ions as allosteric regulators of calmodulin”. In: *J. Biol. Chem.* 260 (1985), pp. 15100–15105.

[72] S. Mocellin and V. Bronte. “Nitric oxide, a double edged sword in cancer biology: searching for therapeutic opportunities.” In: *Med Res Rev* 27.3 (2007), pp. 317–352.

[73] Matias Moller et al. “Direct Measurement of Nitric Oxide and Oxygen Partitioning into Liposomes and Low Density Lipoprotein”. In: *The Journal of Biological Chemistry* 280.10 (2005), pp. 8850–8854.

[74] Sohji Nagase et al. “A Novel Nonenzymatic Pathway for the Generation of Nitric Oxide by the Reaction of Hydrogen Peroxide and D- or L-Arginine”. In: *Biochem. and Biophys. Res. Com.* 233 (1997), pp. 150–153.

[75] Castano A. P., T. N. Demidova, and et al. “Mechanisms in photodynamic therapy: part one-photosensitizer, photochemistry and cellular localization”. In: *Photodiagnosis and Photodynamic Therapy* 1 (2005), pp. 279–293.

[76] Biswaranjan Pani and Brij B Singh. “Lipid rafts/caveolae as microdomains of calcium signaling”. In: *Cell Calcium* 45.6 (2010), pp. 625–633.

[77] J. Parkash and K. Asotra. “Calcium wave signaling in cancer cells.” In: *Life Sci* 87.19-22 (2010), pp. 587–595.

[78] A. Persechini and P. M. Stemmer. “Calmodulin is a limiting factor in the cell”. In: *Trends Cardiovasc. Med.* 12 (2002), pp. 32–37.

[79] Anthony Persechini, Howard D. White, and Krista J. Gansz. “Different Mechanisms for Ca2+ Dissociation from Complexes of Calmodulin with Nitric Oxide Synthase or Myosin Light Chain Kinase”. In: *J. Biol. Chem.* 271.1 (1996), pp. 62–67.

[80] K. Plaetzer et al. “Photophysics and photochemistry of photodynamic therapy: fundamental aspects”. In: *Lasers in Medical Science* 24.2 (2009), pp. 259–268.

[81] S. Porasuphatana et al. “Involvement of the perferryl complex of nitric oxide synthase in the catalysis of secondary free radical formation.” In: *Biochim Biophys Acta.* 1526.1 (2001), 95–104.

[82] Kevin M. Prise and Joe M. O’Sullivan. “Radiation-induced bystander signalling in cancer therapy”. In: *Nature Reviews Cancer* 9.5 (2010), pp. 351–360.

[83] V. Rapozzi, E. Della Pietra, et al. “Nitric oxide-mediated activity in anti-cancer photodynamic therapy.” In: *Nitric Oxide* 30 (2013), pp. 26–35.

[84] A. Rengasamy and R. A. Johns. “Determination of Km for oxygen of nitric oxide synthase isoforms”. In: *J. Pharmacol. Exp. Ther.* 276 (1996), pp. 30–33.

[85] L. D. Robb-Gaspers and A. P. Thomas. “Coordination of Ca2+ signaling by intercellular propagation of Ca2+ waves in the intact liver.” In: *J Biol Chem* 270.14 (1995), pp. 8102–8107.

[86] Kakiuchi S. et al. “Quantitative determinations of calmodulin in the supernatant and particulate fractions of mammalian tissues”. In: *J Biochem.* 92.4 (1982), pp. 1041–1048.

[87] Moncada S, Palmer RM, and Higgs EA. “Nitric oxide: physiology, pathophysiology, and pharmacology”. In: *Pharmacol Rev.* 43.2 (1991), pp. 109–142.

[88] Jerome Santolini. “The molecular mechanism of mammalian NO-synthases: A story of electrons and protons”. In: *Journal of Inorganic Biochemistry* 105 (2011), 127–141.

[89] Jerome Santolini, J. Meade, and Dennis J. Stuehr. “Differences in three kinetic parameters underpin the unique catalytic profiles of nitric-oxide synthases I, II, and III.” In: *J. Biol. Chem.* 276.2 (2001), 48887– 48898.

[90] Jürgen S. Scheele et al. "Kinetics of NO Ligation with Nitric-oxide Synthase by Flash Photolysis and Stopped-flow Spectrophotometry". In: *J. Biol. Chem.* 274 (1999), pp. 13105–13110.

[91] Valter H.C. Silva et al. "Theoretical investigation of nitric oxide interaction with aluminum phtalocyanine". In: *Journal of Molecular Graphics and Modelling* 29 (2011), pp. 777–783.

[92] Nikolai Slavov, Jannette Carey, and Sara Linse. "Calmodulin Transduces Ca2+ Oscillations into Differential Regulation of Its Target Proteins". In: *ACS Chem. Neurosci.* 4 (2013), pp. 601–612.

[93] S.H. Snyder S.R. Jaffrey. "Nitric oxide: a neural messenger". In: *Annu. Rev. Cell Dev. Biol.* 11 (1995), pp. 417–440.

[94] D. J. Stuehr and N. S. Kwon. "N omega-hydroxy-L-arginine is an intermediate in the biosynthesis of nitric oxide from L-arginine". In: *J. Biol. Chem.* 266.10 (1991), pp. 6259–6263.

[95] Dennis J. Stuehr et al. "Update on Mechanism and Catalytic Regulation in the NO Synthases". In: *J. Biol. Chem.* 279.35 (2004), 36167–36170.

[96] Douglas D. Thomas et al. "The biological lifetime of nitric oxide: Implications for the perivascular dynamics of NO and O2". In: *PNAS* 98.1 (2001), pp. 355–360.

[97] Edy Tiravanti, Alexandre Samouilov, and Jay L. Zweier. "Evidence of nitrite-derived nitric oxide formation, storage, and signaling in post-ischemic tissues". In: *J. Biol. Chem.* 279 (2004), pp. 11065–11073.

[98] A. G. Tsai et al. "Oxygen distribution and respiration by the microcirculation." In: *Antioxid. Redox Signal.* 6 (2004), pp. 1011–1018.

[99] Roger Y. Tsien. "A non-disruptive technique for loading calcium buffers and indicators into cells". In: *J. Biol. Chem.* 290.5806 (1981), pp. 527–528.

[100] E. Vacchelli, I. Vitale, et al. "Trial Watch: Anticancer radioimmunotherapy." In: *Oncoimmunology* 2.9 (2013), pp. 255–295.

[101] Rien van Haperen et al. "Functional Expression of Endothelial Nitric Oxide Synthase Fused to Green Fluorescent Protein in Transgenic Mice". In: *American Journal of Pathology* 163.4 (2003), pp. 1677–1686.

[102] N. Vukosavljevic et al. "Quantifying the L-arginine paradox in vivo." In: *Microvasc. Res.* 71 (2006), pp. 48–54.

[103] Z-Q Wang and D J Stuehr. "Calcium Signaling: NO Synthase". In: *Encyclopedia of Biological Chemistry*. Ed. by William J. Lennarz and M. Daniel Lane. Vol. 1. Elsevier, 2013, pp. 342–346.

[104] T.D. Warner et al. "Effects of cyclic GMP on smooth muscle relaxation". In: *Adv. Pharmacol.* 26 (1994), pp. 171–194.

[105] C.C. Wei et al. "A tetrahydrobiopterin radical forms and then becomes reduced during Nomega-hydroxyarginine oxidation by nitric-oxide synthase." In: *J. Biol. Chem.* 278.47 (2003), pp. 46668–73.

[106] A. Weigert and B. Brune. “Nitric oxide, apoptosis and macrophage polarization during tumor progression.” In: *Nitric Oxide* 19.2 (2008), pp. 95–102.

[107] G. Wu and S. M. Jr. Morris. “Arginine metabolism: nitric oxide and beyond.” In: *Biochem. J.* 336 (1998), pp. 1–17.

[108] Pei-Rung Wu et al. “Lobe-Specific Calcium Binding in Calmodulin Regulates Endothelial Nitric Oxide Synthase Activation”. In: *PLOSone* 7.6 (2012), pp. 1–11.

[109] F. Figueroa Xavier et al. “Diffusion of nitric oxide across cell membranes of the vascular wall requires specific connexin-based channels”. In: *Neuropharmacology* 75 (2013), pp. 471–478.